



**1 Impacts of absorbing aerosol deposition on snowpack and hydrologic**  
**2 cycle in the Rocky Mountain region based on variable-resolution**  
**3 CESM (VR-CESM) simulations**

4 Chenglai Wu<sup>1,2</sup>, Xiaohong Liu<sup>1,\*</sup>, Zhaohui Lin<sup>2,3</sup>, Stefan R. Rahimi-Esfarjani<sup>1</sup>, and  
5 Zheng Lu<sup>1</sup>

6 <sup>1</sup>*Department of Atmospheric Science, University of Wyoming, Laramie, Wyoming,*  
7 *USA*

8 <sup>2</sup>*International Center for Climate and Environment Sciences, Institute of Atmospheric*  
9 *Physics, Chinese Academy of Sciences, Beijing, China*

10 <sup>3</sup>*University of Chinese Academy of Sciences, Beijing, China*

11

12 *\*Corresponding to:*

13 Xiaohong Liu  
14 Department of Atmospheric Science  
15 University of Wyoming  
16 Dept. 3038, 1000 East University Avenue  
17 Laramie, WY 82071  
18 Email: [xliu6@uwyo.edu](mailto:xliu6@uwyo.edu).

19

20



## 21 Abstract

22 Deposition of light-absorbing aerosols (LAAs) such as black carbon (BC) and dust  
 23 onto snow cover has been suggested to reduce the snow albedo, and modulate the  
 24 snowpack and consequent hydrologic cycle. In this study we use the  
 25 variable-resolution Community Earth System Model (VR-CESM) with a regionally  
 26 refined high-resolution ( $0.125^\circ$ ) grid to quantify the impacts of LAAs in snow in the  
 27 Rocky Mountain region during the period of 1981-2005. We first evaluate the model  
 28 simulation of LAA concentrations both near the surface and in snow, and then  
 29 investigate the snowpack and runoff changes induced by LAAs in snow. The model  
 30 simulates similar magnitudes of near-surface atmospheric dust concentrations as  
 31 observations. Although the model underestimates near-surface atmospheric BC  
 32 concentrations, the simulated BC-in-snow concentrations are overall comparable to  
 33 observations. Regional mean surface radiative effect (SRE) due to LAAs in snow  
 34 reaches up to  $0.6\text{--}1.7\text{ W m}^{-2}$  in spring, and dust contributes to about 21-43% of total  
 35 SRE. Due to positive snow-albedo feedbacks induced by the LAAs' SRE, snow water  
 36 equivalent reduces by 2-50 mm and snow cover fraction by 5-20% in the two regions  
 37 around the mountains (Eastern Snake River Plain and Southwestern Wyoming),  
 38 corresponding to an increase of surface air temperature by  $0.9\text{--}1.1^\circ\text{C}$ . During the snow  
 39 melting period, LAAs accelerate the hydrologic cycle with monthly runoff increases  
 40 of  $0.15\text{--}1.00\text{ mm day}^{-1}$  in April-May and reductions of  $0.04\text{--}0.18\text{ mm day}^{-1}$  in  
 41 June-July in the mountainous regions. Of all the mountainous regions, Southern



42 Rockies experience the largest reduction of total runoff by 15% during the later stage  
43 of snow melt (i.e., June and July). Our results highlight the potentially important role  
44 of LAA interactions with snowpack and subsequent impacts on the hydrologic cycles  
45 across the Rocky Mountains.

46

## 47 1. Introduction

48 Water resources are essential to human society and economic development as  
49 well as ecosystems in the western United States. Most of primary water resources in  
50 the inland western U.S. come from the Rocky Mountains' snowpack (Serreze et al.,  
51 1999). Therefore, to develop the water resource management strategy, it is necessary  
52 to know the information of snow accumulation and snowmelt timing. Climate change  
53 is an important factor influencing the snowpack in the Rocky Mountain region, as has  
54 been shown in many previous studies (e.g., Abatzoglou, 2011; Pederson et al., 2011;  
55 Rhoades et al., 2017). Another important factor is the light-absorbing aerosols (LAAs,  
56 e.g., black carbon (BC), organic carbon (OC), and dust) in snow (e.g., Flanner et al.,  
57 2007; Painter et al., 2007; Qian et al., 2015; Yasunari et al., 2015). Previous studies  
58 have shown that LAAs in snow can significantly reduce the surface albedo (often  
59 known as snow darkening effect (SDE)), modify the surface energy budget and  
60 snowmelt, and lead to the modification of hydrologic cycles (e.g., Warren and  
61 Wiscombe, 1980; Hansen and Nazarenko, 2004; Flanner et al., 2007, 2009; Painter et  
62 al., 2007, 2010; Qian et al., 2009, 2011; Yasunari et al., 2015). Moreover, the



63 LAAs-induced snow albedo reduction may initiate positive feedback processes, which  
64 can amplify the reduction of snowpack (e.g., Flanner et al., 2009; Qian et al., 2009).

65 In past decades modeling studies have been undertaken to quantify the impacts  
66 of SDE by LAAs (e.g., Flanner et al., 2007; Qian et al., 2009; Oaida et al., 2015;  
67 Yasunari et al., 2015). Generally the models they developed have the ability to  
68 simulate the temporal evolution of snow albedo under the influence of LAAs in snow.  
69 These studies have enhanced our understanding of the spatial and temporal variations  
70 of climate forcings and responses due to LAAs in snow from regional scales (e.g.,  
71 Qian et al., 2009; Oaida et al., 2015) to global scales (e.g., Flanner et al., 2007;  
72 Yasunari et al., 2015). For example, the impacts of LAAs in snow are stronger in  
73 regions with considerable snow cover and sufficient LAAs deposition (e.g., Arctic,  
74 Northeast China, Tibetan Plateau, and western U.S.) than in other regions, and they  
75 are largest during the snowmelt period due to the positive snow-albedo feedback.  
76 However, as also mentioned in these studies, reliable quantification of impacts of  
77 LAAs in snow is hindered by the model deficiencies in simulating the snowpack and  
78 aerosol cycles, with additional uncertainties induced by the parameterization of  
79 snow-aerosol-radiation interactions.

80 In particular, previous studies used the coarse-resolution global climate  
81 models (GCMs) or high-resolution regional climate models (RCMs) to quantify the  
82 impacts of LAAs in snow. However, there are weaknesses in either coarse-resolution  
83 GCMs or RCMs. Both snowfall and snow accumulation depend on the temperature



84 and precipitation, and thus distribution of snowpack depends strongly on topographic  
85 variability. Current GCMs with a typical horizontal resolution of  $1^\circ$  to  $2^\circ$  cannot  
86 resolve the snowpack over the regions with complex terrains (e.g., Rocky Mountains)  
87 due to the coarse resolution (Rhoades et al., 2016; Wu et al., 2017), which impedes  
88 the reliable quantifications of SDE by LAAs in mountainous regions (e.g., Flanner et  
89 al., 2007; Yasunari et al., 2015). For RCMs, they can simulate the snowpack more  
90 accurately but are not able to simulate the global transport of aerosols to the focused  
91 region except that aerosol transport along the boundary is prescribed (e.g., Qian et al.,  
92 2009; Oaida et al., 2015). Moreover, LAAs in snow may also influence the climate  
93 beyond the focused region (e.g., Yasunari et al., 2015), which cannot be accounted for  
94 in RCMs. Variable resolution GCMs (VR-GCMs) can overcome these weaknesses of  
95 either coarse-resolution GCMs or RCMs and serve as a better tool to quantify the  
96 impacts of LAAs in snow. Although GCMs with globally uniform high resolutions  
97 (10-30 km) may be an ideal tool to simulate the snowpack and snow-aerosol-radiation  
98 interactions, they are not widely applied due to the constraints of computational  
99 resources (e.g., Haarsma et al., 2016). Instead, using VR-GCMs is a more economic  
100 approach and has gained increasing utility in recent years (e.g., Zarzycki et al, 2014a,  
101 b; Sakaguchi et al., 2015).

102 A variable-resolution version of the Community Earth System Model  
103 (VR-CESM) has been developed (Zarzycki et al., 2014a, b). With a refined high  
104 resolution, VR-CESM has shown significant improvements of the Atlantic tropical



105 storms (Zarzycki and Jablonowski, 2014) and South America orographic precipitation  
106 (Zarzycki et al., 2015). The model has also been used in the regional climate  
107 simulations in western U.S., and results show that VR-CESM is capable of  
108 reproducing the spatial patterns and the seasonal evolution of temperature,  
109 precipitation, and snowpack in Sierra Nevada (Huang et al., 2016; Rhoades et al.,  
110 2016) and in Rocky Mountains (Wu et al., 2017). In particular, VR-CESM simulates  
111 reasonably the magnitude of snow water equivalent, the timing of snow water  
112 equivalent peaks, and the duration of snow cover in the Rocky Mountains by  
113 comparing against the Snow Telemetry (SNOTEL) and MODIS (Moderate  
114 Resolution Imaging Spectroradiometer) snow cover observations (Wu et al., 2017).

115       Following the evaluation study of Wu et al. (2017), here we use VR-CESM to  
116 investigate the impacts of LAAs in snow (BC and dust) on the snowpack and  
117 hydrologic cycles over the Rocky Mountains. By comparing the two VR-CESM  
118 simulations with and without considering the impacts of LAAs in snow, we examine  
119 the changes in surface radiative transfer, temperature, snowpack, and runoff induced  
120 by LAAs in snow. To our knowledge, it is the first time that VR-CESM is applied for  
121 the study of LAAs in snow. Our results will demonstrate that VR-CESM is skillful for  
122 this kind of research.

123       The remainder of the paper is organized as follows. Section 2 introduces the  
124 model and experimental design. Section 3 describes the observation data used for  
125 validation of model simulations of aerosol fields in the surface air and in snow.



126 Section 4 presents the evaluation of aerosols fields, followed by their surface radiative  
127 effect (SRE), as well as the change of surface temperature, snowpack, and runoff  
128 induced by LAAs in snow. Discussion and conclusions are given in section 5.

## 129 2. Model and experimental design

130 The model used in this study is VR-CESM, a version of CESM (version 1.2.0)  
131 with the variable-resolution capability (Zarzycki et al., 2014a, b). CESM is a  
132 state-of-the-art Earth system modeling framework that allows for investigations of  
133 a diverse set of Earth system interactions across multiple time and space scales  
134 (Hurrell et al., 2013). CESM uses the Community Atmosphere Model version 5  
135 (CAM5) for the atmospheric component (Neale et al., 2010). The variable-resolution  
136 capability is implemented into the Spectral Element (SE) dynamic core of CAM5.  
137 The SE dynamic core uses a continuous Galerkin spectral finite-element method  
138 designed for fully unstructured quadrilateral meshes, and has demonstrated  
139 near-optimal (close to linear) parallel scalability on tens of thousands of cores (Dennis  
140 et al., 2012). This enables the model to run efficiently on decadal to multi-decadal  
141 time scales. For the land component, CESM uses the Community Land Model version  
142 4 (CLM4). CLM4 can be run at the same horizontal resolutions as CAM5 and thus  
143 also benefit from the variable-resolution capability of CAM5.

144 CESM also includes advanced physics for CAM5 (Neale et al., 2010) and  
145 CLM4 (Oleson et al., 2010). The CAM5 physics suite consists of shallow convection  
146 (Park and Bretherton, 2009), deep convection (Zhang and McFarlane, 1995; Richter



147 and Rasch, 2008), cloud microphysics (Morrison and Gettelman 2008) and  
148 macrophysics (Park et al. 2014), radiation (Iacono et al. 2008), and aerosols (Liu et al.,  
149 2012). For aerosols, a modal aerosol module (MAM) is adopted to represent the  
150 internal and external mixing of aerosol components such as BC, OC, sulfate,  
151 ammonium, sea salt, and mineral dust (Liu et al., 2012). CLM4 physics includes a  
152 suite of parameterizations for land-atmosphere exchange of water, energy and  
153 chemical compounds. In particular, CLM4 explicitly represents the snowpack (snow  
154 accumulation and melt) by a snow model and its coupling with the SNow, Ice and  
155 Aerosol Radiation (SNICAR) model for snow-aerosol-climate interactions (Flanner et  
156 al., 2007). SNICAR incorporates a two-stream radiative transfer solution of Toon et  
157 al. (1989) to calculate the snow albedo and the vertical absorption profile from solar  
158 zenith angle, albedo of the substrate underlying snow, mass concentrations of  
159 atmospheric-deposited aerosols (BC and dust), and ice effective grain size ( $r_e$ ).  $r_e$  is  
160 simulated with a snow aging routine (Oleson et al., 2010). SNICAR is compatible  
161 with the new modal aerosol module of CAM5 (Liu et al., 2012) in the treatment of  
162 aerosol deposition (Flanner et al., 2012). As our knowledge of OC optical properties  
163 is limited, the impact of absorbing OC on snow albedo is not included in the standard  
164 CLM4 and thus not considered in this study.

165 For the high-resolution modeling, we have designed a variable-resolution grid  
166 that transits from global quasi-uniform  $1^\circ$  resolution to a refined  $0.125^\circ$  resolution in  
167 the Rocky Mountains (Figure 1a). The variable-resolution grid is the same as that





168 used in Wu et al. (2017), and is generated by the open-source software package called  
169 SquadGen (Ullrich, 2014). A topographical dataset for this variable-resolution grid is  
170 also generated accordingly by the National Center for Atmospheric Research (NCAR)  
171 global model topography generation software called NCAR\_Topo (v1.0) (Lauritzen et  
172 al., 2015) as described in Wu et al. (2017). As shown in Figure 1b, the high-resolution  
173 grids resolve well the variations of terrain in the Rocky Mountains. Note that the  
174 standard CESM using the coarse  $1^\circ$  grids cannot resolve the fine-scale variations of  
175 terrain in the Rocky Mountains (see Figure 2 of Wu et al. (2017)). In Wu et al. (2017),  
176 we have shown that VR-CESM performs well in the simulation of regional climate  
177 patterns, including spatial distributions and seasonal evolution of temperature,  
178 precipitation, and snowpack in the Rocky Mountain region. In this study, we further  
179 apply VR-CESM to simulate the SDE of LAAs and its impacts on snowpack and  
180 hydrologic cycles in the Rocky Mountains.

181 VR-CESM is run in the coupled land-atmosphere mode with prescribed  
182 observed monthly  $1^\circ \times 1^\circ$  sea surface temperature and sea ice coverage (Hurrell et al.,  
183 2008), following the Atmospheric Model Intercomparison Project (AMIP) protocols  
184 (Gates, 1992). The simulation period is from 1979 to 2005, and the results for the last  
185 25 years (1981-2005) are used for the analysis shown below. Historical greenhouse  
186 gas concentrations, and anthropogenic aerosol and precursor gas emissions are  
187 prescribed from the datasets of Lamarque et al. (2010). In particular, the BC  
188 emissions consist of various sources, including domestic, energy, transportation,



189 waste, shipping, and wildfire (forest and grass fires) emissions. We note that the  
190 horizontal resolution for BC emission used in this study is  $1.9 \times 2.5^\circ$ . The relatively  
191 coarse resolution of BC emission may partly explain the model's bias in the  
192 simulation of BC concentrations near the surface and in snow across regions where  
193 local BC sources can contribute significantly to the observed BC concentrations, as  
194 will be discussed in section 4.

195 For dust aerosol, the emission flux is calculated interactively in the model at  
196 each time step by a dust emission scheme (Oleson et al., 2010). The dust emission  
197 flux is calculated from the friction velocity, threshold friction velocity, atmospheric  
198 density, clay content in the soil, areal fraction of exposed bare soil, and source  
199 erodibility (Oleson et al., 2010; Wu et al., 2016). Due to the large uncertainty in  
200 modeled dust emission, the dust emission scheme also adopts a posterior tuning factor  
201 ( $T$ ) to simulate the reasonable dust emission amount. With the increase of model  
202 resolution, VR-CESM produces much higher dust concentrations compared to the  
203 observations (section 3) in North America if  $T$  used in the standard CESM with  
204 quasi-uniform  $1^\circ$  resolution is used. Therefore, for VR-CESM,  $T$  is reduced by a  
205 factor of 2.6 to produce the similar magnitudes of near-surface dust concentrations as  
206 the observations, as will be shown in section 4.1. Note that such a reduction of  $T$  is  
207 only applied in North America, since other continents have a resolution of  
208 quasi-uniform  $1^\circ$ , the same as in the standard CESM.



209           In addition to the control experiment with the impacts of LAAs (BC and dust)  
210   in snow included (CTL), we conduct a sensitivity experiment that turns off the impact  
211   of LAAs in snow (NoSDE). Through the comparison of these two simulations (CTL  
212   and NoSDE), the impacts of SDE by LAAs on the snowpack and hydrologic cycles  
213   can be identified. To facilitate the analysis of SDE, we also calculate the surface  
214   radiative effect (SRE) by BC (dust) in snow in the control experiment from the  
215   difference of absorbed radiation with all aerosols (i.e., the standard radiation call) and  
216   with all aerosols except BC (dust) as Flanner et al. (2007) (a diagnostic radiation call).

217           To quantify the impacts of LAAs in snow, we mainly focus on the five regions.  
218   Three of these regions are in the high mountains: Northern Rockies, Greater  
219   Yellowstone region, and Southern Rockies. The elevation is higher in Greater  
220   Yellowstone region and Southern Rockies (>2250 m) than in Northern Rockies (>750  
221   m). The other two regions are over the plains near the mountains: Snake River Basin  
222   and Southwestern Wyoming. These two regions are selected because they are close to  
223   the source regions of BC and dust and also have considerable snow cover (>50%) in  
224   winter. These five regions are shown in Figure 1c.

### 225   **3. Observations**

226           We will use various observations to validate the model simulation of aerosol  
227   (BC and dust) concentrations near the surface and in snow.

228           First, we use the observations of near-surface BC and dust concentrations from  
229   the Interagency Monitoring of PROtected Visual Environments (IMPROVE) network



230 (Malm et al., 1994). Observed mass concentrations of Elemental Carbon (EC) are  
231 used for the comparison with model simulation of BC concentrations. Although EC  
232 can be somewhat different from BC (Andreae and Gelencser, 2006), EC  
233 concentrations have been widely used for the validation of BC concentrations in  
234 previous studies (e.g., Koch et al., 2009; Liu et al., 2012). For dust, simulated dust  
235 concentration accounts for dust particles with diameters below 10  $\mu\text{m}$ . To compare,  
236 observed mass concentrations of fine soil (FS, with the diameter  $<2.5 \mu\text{m}$ ) and coarse  
237 mass (CM, with the diameter between 2.5  $\mu\text{m}$  and 10  $\mu\text{m}$ ) from IMPROVE are  
238 combined, following the approach of Kavouras et al. (2007) and Wells et al. (2007).  
239 In reality, in addition to dust, CM may also contain other aerosols such as sulfate,  
240 nitrate, organic and elemental carbon, and sea salt. However, according to the study of  
241 Malm et al. (2007), who analyzed the speciation of coarse particles collected at nine  
242 selected rural IMPROVE stations in 2004, the contributions of dust to CM are above  
243 70% (74-90%) in the three stations in inland western U.S. In their study, lower  
244 contributions of dust to CM (34% and 65%) were found in the two stations near the  
245 coast. We caution that these two stations were  $<150 \text{ km}$  away from the metropolitan  
246 regions indicating that urban emissions may also contribute to CM there. Additional  
247 contributions may result from sea salt or sodium nitrate resulting from reactions of  
248 nitric acid with sea salt, as mentioned in their study (Malm et al., 2007). Therefore, to  
249 minimize the contributions of other aerosols to CM, we do not use the stations in or  
250 near the metropolitan regions or near the coast for the validation of dust concentration.



251 Nonetheless, we acknowledge that there may be small contributions from other  
252 aerosols to CM and the estimated dust concentration by summing FS and CM may  
253 represent an upper limit of dust concentrations (with the diameter  $<10\ \mu\text{m}$ ) from the  
254 observations. Note that the observation period of IMPROVE varies with the stations,  
255 some stations started earlier in 1980s, and some from more recently (2000s). To  
256 derive a climatological dataset for model comparisons, we only select the stations  
257 with more than 5 years of dust observations. Totally there are 80 and 94 stations for  
258 BC and dust observations, respectively, in the western U.S. (Figure 2).

259 Second, we collect the field measurements of BC mass concentrations in snow  
260 ( $C_{\text{BC}}$ ) from previously published studies. Although field observations of  $C_{\text{BC}}$  in snow  
261 extended back to 1980s, they were made mostly in high-latitudes, Alps Mountains,  
262 Cascade Mountains, eastern Canada, and West Texas/New Mexico (see Qian et al.  
263 (2015) and references therein). Recently, Doherty et al. (2014) made valuable  
264 measurements of the vertical profiles of LAAs in seasonal snow from January to  
265 March of 2013. They used an Integrating Sphere integrating SandWich (ISSW)  
266 Spectrophotometer to estimate the BC mixing ratios in snow over 67 sites in North  
267 America (including 17 sites in the Rocky Mountain region). Observed  $C_{\text{BC}}$  by  
268 Doherty et al. (2014) was recorded on a single day. Doherty et al. (2016) further  
269 provided the temporal variations of  $C_{\text{BC}}$  at four stations, three at Idaho (January to  
270 March of 2014) and one at Utah (February to March of 2013 and 2014). Doherty et al.  
271 (2016) also calibrated the ISSW measurements using an incandescence technique (the



272 Single Particle Soot Photometer, SP2) in a subset of the observations, which was  
273 supposed to capture  $C_{BC}$  more accurately, and derived a ratio of  $C_{BC}$  by ISSW to  $C_{BC}$   
274 by SP2 based on their linear relationship for the estimation of real  $C_{BC}$ . This  
275 calibration is applied to the dataset of Doherty et al. (2014) in our study, and thus the  
276 observations of Doherty et al. (2014) and Doherty et al. (2016) are comparable and  
277 used here.

278 In addition, Skiles and Painter (2016b) made daily measurements of  
279 BC-in-snow with SP2 in the Senator Beck Basin Study Area (SBBSA) in the San  
280 Juan Mountains during a period of two month (late March to middle May) in 2013.  
281 The locations and sample dates as well as the measurements for these stations are  
282 given in Table 1. If measurements of  $C_{BC}$  on multiple days were made, the means and  
283 standard deviations of  $C_{BC}$  are given. As our simulation period does not encompass  
284 the years 2013 and 2014, we will compare the monthly mean results for 25 years  
285 (1981-2005) by focusing more on the general magnitudes and spatial distributions of  
286  $C_{BC}$ . At each station, the mean results for the month (or months) when the  
287 observations were made, as well as the maximum and minimum  $C_{BC}$ , are derived  
288 from the 25-year simulation and compared to the observations.

289 Third, for dust, there are few observations of dust mass mixing ratio in snow  
290 ( $C_{dust}$ ) in the Rocky Mountain region. To our best knowledge, the only published  
291 observations were conducted in the Senator Beck Basin Study Area (SBBSA) in the  
292 San Juan Mountains (in Southern Rockies) with at least 9-year (2005-2013) records



(Painter et al., 2007, 2012; Skiles and Painter, 2016a, 2016b). Snow samples at a depth of 30 cm were collected at irregular time intervals for each dust event from March to May. We will compare simulated  $C_{\text{dust}}$  for the whole snow columns with the observations (for 0-30 cm depth), but acknowledge that  $C_{\text{dust}}$  may vary in the snow underneath 0-30 cm snow layer. Another consideration is that observed  $C_{\text{dust}}$  contains all the dust particles while simulated  $C_{\text{dust}}$  only accounts for the dust particles with diameters smaller than 10  $\mu\text{m}$ . According to the observations of Reynolds et al. (2016), the concentration of total suspended particles (TSP) in the atmosphere is mainly contributed from particles with diameters larger than 10  $\mu\text{m}$ . This will affect the model comparison with the observations, which will be discussed in section 4.

## 4. Results

### 4.1 Spatial patterns of near-surface aerosol concentrations

Before we examine the impacts of aerosol deposition onto snow, we will first evaluate the aerosol simulations by the model. Figure 2 shows the spatial patterns of cold season (winter and spring) mean emission fluxes and near-surface concentrations of BC and dust in the western U.S. from the VR-CESM simulation. The IMPROVE stations are also denoted by cycles with larger cycle sizes indicating higher observed near-surface BC/dust concentrations. In the model, the BC emission flux is prescribed and is largest in the Pacific Coast and southern Arizona. BC emission fluxes are relatively large in central–northern Colorado and Northwestern Utah, where large metropolises are located. Corresponding to the patterns of BC emission flux,



314 simulated near-surface BC concentrations ( $>100 \text{ ng m}^{-3}$ ) are also higher in these  
315 regions. A band with relatively high near-surface BC concentrations around 50-100  
316  $\text{ng m}^{-3}$  is also found in southern Idaho, to the west of the Greater Yellowstone region  
317 and to the south of Northern Rockies, indicating the transportation of BC around the  
318 mountains. Near-surface BC concentrations decrease at higher elevations. The spatial  
319 patterns simulated by the model are generally consistent with observations, e.g.,  
320 higher BC concentrations in the source regions and lower in the mountains.

321 Dust sources are located in the dry regions with exposed bare soils, such as the  
322 southwestern U.S. (southern California, western Arizona, and southern New Mexico),  
323 the northern Mexico, the Great Basin, and the Colorado Plateau. Dust emissions are  
324 also found in the Great Plains, although it is much weaker. In the Great Plains  
325 agricultural activities can disturb the soil, making it vulnerable to wind erosion  
326 (Ginoux et al., 2012). Simulated cold season mean dust concentrations are higher  
327 ( $10\text{-}500 \text{ } \mu\text{g m}^{-3}$ ) in the source regions, but decrease dramatically ( $0.1\text{-}5 \text{ } \mu\text{g m}^{-3}$ ) to the  
328 mountains. Compared to the observations, the model reproduces the spatial patterns of  
329 near-surface dust concentrations with higher concentrations in the southwestern part  
330 of US. However, the model tends to overestimate the dust concentrations in Utah,  
331 indicating that dust emission may be overestimated there.

332 Comparisons of modeled and observed near-surface BC/dust concentrations at  
333 the IMPROVE stations are further shown in Figure 3. Overall, the model captures the  
334 magnitudes of observed near-surface BC and dust concentrations with the differences





335 between observations and simulations within a factor of 5 for most of the stations.  
336 The model simulates similar magnitudes of observed near-surface BC concentrations  
337 at the stations along the West Coast and in the Southwestern U.S. However, the model  
338 tends to underestimate observed near-surface BC concentrations in Utah–Nevada  
339 regions, the Rocky Mountains, and the Great Plains, where the stations are located in  
340 the downwind of source regions (Figure 2b). In particular, observed near-surface BC  
341 concentrations are underestimated by about a factor of two in the Rocky Mountains.  
342 The underestimation of near-surface BC concentrations in these regions may suggest  
343 that transport of BC in our simulations is too weak. This deficiency may also be  
344 ascribed to the local BC sources (e.g., Doherty et al., 2014) not resolved by the  
345 prescribed BC emission in the model (e.g., at  $1.9\times 2.5^\circ$  resolution). For dust, although  
346 the model overestimates near-surface dust concentrations for most of the stations near  
347 the dust sources (southwestern U.S., Utah, and Nevada), the model simulates well the  
348 magnitude of near-surface dust concentrations in the Rocky Mountains. This may also  
349 be associated with underestimated transport in the model, as indicated in the bias of  
350 near-surface BC concentrations in the downwind regions.

351 Note that although only the BC and dust emission fluxes over the western U.S.  
352 are shown in Figure 2, long-range transport of these aerosols from other regions (e.g.,  
353 Asia and Africa) can also contribute to BC (e.g., Zhang et al., 2015) and dust (Wells  
354 et al., 2007) concentrations in the western U.S. Meanwhile, there are also substantial  
355 variations of aerosol emission in the western U.S. As mentioned in section 2, although



we adopt VR-CESM with a refined high resolution ( $0.125^\circ$ ) in the Rocky Mountains, we use a coarse resolution gridded emission dataset (i.e.,  $1.9^\circ \times 2.5^\circ$ ) for BC. For dust, the small-scale variations of dust emission can be represented in the model as it is calculated online in the model. However, dust emission depends on many variables such as near-surface winds, soil moisture, vegetation cover, and soil texture (Oleson et al., 2010; Wu et al., 2016), which may be biased. In particular, in Utah and Nevada, simulated near-surface dust concentrations are about 2-3 times as large as observations, indicating the significant overestimation of dust emission in the region. Despite the aforementioned biases, the model does reasonably well in the simulation of spatial variations of near-surface BC and dust concentrations in western U.S.

#### 4.2 Aerosol-in-snow concentrations

Figure 4 shows the spatial distributions of BC and dust mass mixing ratios in snow in winter and spring from VR-CESM simulations. BC-in-snow mass mixing ratio in the Rocky Mountains ranges from  $2\text{--}50\text{ ng g}^{-1}$ , which is consistent with a previous study (Qian et al., 2009). The dust-in-snow mass mixing ratio ( $0.1\text{--}50\text{ }\mu\text{g g}^{-1}$ ) is about 2-3 orders of magnitude higher than that of BC-in-snow. The spatial pattern of BC-in-snow mixing ratios is consistent with that of near-surface atmospheric BC concentration, which features higher values in northern Utah and southern Idaho and lower values in the higher mountains (Figure 2b). Dust-in-snow mixing ratios are higher in Utah and downwind regions (western Colorado and southern Idaho), which is consistent with the distribution of near-surface atmospheric dust concentrations.



377 Dust-in-snow mixing ratio is also higher in the northern Great Plains, where dust  
378 emission is also evident (Figure 2c). In addition, BC and dust mixing ratios are larger  
379 ( $10\text{--}100\text{ ng g}^{-1}$  and  $2\text{--}50\text{ }\mu\text{g g}^{-1}$ , respectively) in the Southern Rockies than in Northern  
380 Rockies and Greater Yellowstone region. BC and dust mass mixing ratios are smaller  
381 in Greater Yellowstone region with ranges from  $10\text{--}50\text{ ng g}^{-1}$  and from  $0.2\text{--}2\text{ }\mu\text{g g}^{-1}$ ,  
382 respectively, and are smallest in the Northern Rockies with the values below  $20\text{ ng g}^{-1}$   
383 and below  $2\text{ }\mu\text{g g}^{-1}$ , respectively. BC and dust mixing ratios in snow are larger in  
384 spring than in winter in most of the Rocky Mountain region. This indicates that BC  
385 and dust accumulate within the snow column during the snow accumulation and the  
386 early portion of the snow melting season.

387 The comparison of BC mass mixing ratios in the snow column at the 17 sites  
388 from VR-CESM simulations and observations is shown in Figure 5. As observations  
389 only sampled the snow in one day or tens of days, simulated mean and standard  
390 deviations of BC-in-snow mass mixing ratios in the same month are given for the  
391 comparison. The months of observations occurred between January and May.  
392 Observed BC-in-snow mass mixing ratios range from  $5.6\text{ ng g}^{-1}$  to  $33.6\text{ ng g}^{-1}$  at the  
393 17 sites. The model reproduces reasonably the magnitude of observed BC-in-snow  
394 mass mixing ratios at most of the stations. The exception is that at the two stations  
395 (sites #15 and #16) where the model significantly underestimates observed  
396 BC-in-snow mass mixing ratios by a factor of more than 5. Site #15 is close to the  
397 sites #13 and #14 and they are all located on the southwestern flanks of Northern



398 Rockiest (Figure 4). Observed BC mass mixing ratios at site #15 ( $14.9 \text{ ng g}^{-1}$ ) is  
399 higher than those at sites #14 ( $13.3 \text{ ng g}^{-1}$ ) and #13 ( $9.8 \text{ ng/g}$ ), which indicates the  
400 northward transport of BC (Doherty et al., 2016). Simulated BC-in-snow mass mixing  
401 ratios are around  $8.8 \text{ ng g}^{-1}$  and  $10.9 \text{ ng g}^{-1}$  at sites #13 and #14, respectively, which  
402 are comparable to the observations. However, the simulated value is only  $2.5 \text{ ng g}^{-1}$  at  
403 site #15. This indicates that the model may lack the ability to simulate the transport  
404 and/or deposition of BC in this region. Site 16 is located in northeastern Utah, where  
405 snow depths are smaller compared to other mountains regions. When snow is melted  
406 completely, BC-in-snow mixing ratio will be zero, but the model will average the  
407 simulation results at different time steps to derive the mean result. In the observations,  
408 only BC-in-snow samples are accounted for. The different sample strategy may partly  
409 explain the difference between the simulations and observations. Another reason may  
410 be that observations show a large interannual variability of BC-in-snow mass mixing  
411 ratios at site #16 and the observation period was not long enough for the derivation of  
412 a climatological mean as in the simulation.

413 Note that although near-surface BC concentrations in the atmosphere are  
414 underestimated in the Rocky Mountains in the model (section 4.1), BC mass mixing  
415 ratios in the snow are not overall underestimated. In our study, we calibrate the  
416 observational data of Doherty et al. (2014) by using the correction factor based on the  
417 comparison of ISSW and SP2, assuming that SP2 can more accurately measure the  
418 mass mixing ratio of BC compared to ISSW (Doherty et al., 2016). However,



419 although SP2 can provide a direct measurement of BC, SP2 may underestimate the  
420 real amount of BC-in-snow mass when BC is attached to larger particles (e.g., dust  
421 and sea salt) or aggregates to large sizes in snow due to the size range (e.g.,  $\sim 0.08\text{--}0.7$   
422  $\mu\text{m}$ ) limitations in SP2 (Qian et al., 2015). Because of this, the real amount of  
423 BC-in-snow mass may be higher than that measured by SP2. Therefore, VR-CESM  
424 may also underestimate the BC-in-snow mass mixing ratios, although the exact degree  
425 of underestimation is unknown. Another reason for the inconsistency of BC mass  
426 mixing ratios in snow and near-surface BC concentrations in the atmosphere may be  
427 related to the snow aging/melting and BC-in-snow accumulation and flushing-out,  
428 which are associated with large uncertainties (Flanner et al., 2007; Qian et al., 2014).

429 For dust in snow, the simulated mean dust mass mixing ratio in snow in spring  
430 is  $19.6 \mu\text{g g}^{-1}$  in the San Juan Mountains. The simulated standard deviation, minimum,  
431 and maximum of dust mass mixing ratios for 1981-2005 are  $22.4 \mu\text{g g}^{-1}$ ,  $5.3 \mu\text{g g}^{-1}$ ,  
432 and  $118.7 \mu\text{g g}^{-1}$ , respectively. This value is one to two orders of magnitude smaller  
433 compared to the observations of Skiles and Painter et al. (2016a), which showed that,  
434 at the end of the snow season, the total dust-in-snow mass mixing ratios range from  
435  $0.2$  to  $4.8 \text{ mg g}^{-1}$ . Much smaller dust-in-snow mass mixing ratios in the simulations  
436 may be ascribed to the fact that the model only accounts for dust particles with  
437 diameters smaller than  $10 \mu\text{m}$ , while the observations include all the sizes of dust  
438 particles in the snow. Actually, an observation made by Reynolds et al. (2016) in the  
439 Utah-Colorado region showed that concentrations of total suspended particles (TSP)



440 in the atmosphere are mainly contributed from larger particles with diameters larger  
441 than 10  $\mu\text{m}$ . Therefore, the model may underestimate the impacts of dust deposition  
442 into snow, and the dust impacts in this study, which will be discussed below, can be  
443 regarded as those from the dust particles with diameters smaller than 10  $\mu\text{m}$ .

#### 444 **4.3 Surface radiative effect (SRE) by aerosol-in-snow**

445 Figure 6 shows the spatial distribution of instantaneous surface radiative effect  
446 (SRE) due to BC- and dust-induced snow albedo change, respectively, in winter  
447 (December-January-February) and spring (March-April-May). Due to the decrease of  
448 surface albedo, surface net shortwave radiation is increased. The spatial patterns of  
449 SRE are determined collectively by both the amount of aerosol-in-snow and the  
450 distribution of snowpack (snow depth and snow cover fraction). Finer-scale structures  
451 of SRE in the Rocky Mountains and the adjacent regions are simulated by VR-CESM  
452 with a higher horizontal resolution compared to previous simulations by  
453 coarse-resolution GCMs (e.g., Flanner et al., 2009; Yasunari et al., 2015). The SRE is  
454 generally above 0.2  $\text{W m}^{-2}$  over the mountains especially in the Greater Yellowstone  
455 region and Southern Rockies. SRE can reach similar magnitudes on the southern  
456 periphery of Northern Rockies and west side of the Greater Yellowstone region,  
457 where higher near-surface atmospheric BC/dust concentrations and BC/dust-in-snow  
458 mass mixing ratios are simulated (Figures 2 and 4). SRE is stronger in spring than in  
459 winter for both BC and dust, which is consistent with previous studies (Flanner et al.,  
460 2009; Yasunari et al., 2015). This is because of the stronger solar insolation and larger



461 albedo reduction due to snow aging and aerosol accumulation within snow in spring.  
462 There are more dust emission and consequent dust transport and deposition in spring  
463 than in winter, which may also partly contribute to the larger dust-induced SRE in  
464 spring than in winter. For different aerosols, BC-induced SRE is somewhat larger than  
465 dust-induced SRE in both winter and spring. BC-induced SRE is mostly below  $1 \text{ W m}^{-2}$   
466  $\text{m}^{-2}$  in winter, but reaches up to  $2\text{-}5 \text{ W m}^{-2}$  in spring. Dust-induced SRE is mostly  
467 below  $0.5 \text{ W m}^{-2}$  in winter and increases to  $1\text{-}5 \text{ W m}^{-2}$  in spring.

468 Compared to those in the Greater Yellowstone region and Southern Rockies,  
469 SRE in the Northern Rockies is much smaller (mostly below  $0.05$  and  $0.5 \text{ W m}^{-2}$  in  
470 winter and spring), because of smaller aerosol-in-snow mass values in this region  
471 (Figure 4). Note that BC-induced SRE is still significant (mostly around  $0.2\text{-}2 \text{ W m}^{-2}$   
472 and  $2\text{-}5 \text{ W m}^{-2}$  in some local regions) in the northern Great Plains, eastern U.S.,  
473 southern Canada, and eastern Canada. This was also shown in previous studies using  
474 coarse-resolution GCMs (e.g., Flanner et al., 2009; Yasunari et al., 2015). In addition,  
475 the model also simulates non-negligible dust-induced SRE (mostly around  $0.05\text{-}0.2 \text{ W}$   
476  $\text{m}^{-2}$  and up to  $0.2\text{-}0.5 \text{ W m}^{-2}$  in some local regions) near the dust sources in southern  
477 Canada and the northern Great Plains.

478 Figure 7 shows the monthly variations of SRE induced by BC and dust SDE in  
479 the five regions (Northern Rockies, Greater Yellowstone region, Southern Rockies,  
480 Eastern Snake River Plain, and Southwestern Wyoming). Table 2 gives the regional  
481 averaged winter and spring SRE in these five regions. Consistent with the spatial



distributions shown in Figure 6, aerosol-induced SRE averaged in Northern Rockies is about half to one-fourth of those in Greater Yellowstone region and Southern Rockies. Compared to that in winter, SRE is much larger in spring, which is a result of aerosol accumulation in snow and relatively strong solar insolation. The peaks of SRE occur in April-May in the three mountainous regions (Northern Rockies, Greater Yellowstone region, and Southern Rockies), which corresponds to the onset of snowmelt after the peaks of snow water equivalent (early-to-middle April; see figure 11 of Wu et al. (2017)). In the Eastern Snake River Basin and Southwestern Wyoming, the peaks of SRE occur in March, which is different from the three mountainous regions because the snowmelt period begins earlier (in February-to-March) in these two regions (section 4.4). Regional mean total SRE in spring induced by BC and dust can reach up to 1.58-1.7 W m<sup>-2</sup> with peaks around 2.0 W m<sup>-2</sup> in Greater Yellowstone region and Southern Rockies. In Eastern Snake River Plain and Southwestern Wyoming, regional mean total SRE in winter and spring is around 0.4-0.6 W m<sup>-2</sup> and 0.7-0.8 W m<sup>-2</sup>, respectively. For the contribution of different aerosols, BC-induced springtime SRE is larger than dust-induced SRE in the five regions. Despite this, dust-induced springtime SRE can still contribute to about 20-30% of total springtime SRE in the northern part of Rocky Mountains (Northern Rockies, Greater Yellowstone region and Eastern Snake River Plain). In the southern part of Rocky Mountains (Southwestern Wyoming and Southern Rockies), dust-induced springtime SRE contributes more significantly (about 30-40%) to total springtime SRE.





#### 503    **4.4 Impacts of aerosol SDE on the surface temperature and snowpack**

504            Figure 8 shows surface air temperature, snow water equivalent, and snow  
505    cover fraction changes due to the aerosol SDE in winter and spring, respectively.  
506    Snow water equivalent is defined as the amount of water contained within the  
507    snowpack, measured by  $\text{kg m}^{-2}$  which is equivalent to mm after dividing the density  
508    of water ( $1000 \text{ kg m}^{-3}$ ). Snow cover fraction is defined as the fraction of surface area  
509    covered by snow. These changes are derived from the difference between two  
510    simulations (CTL and NoSDE). The crosses in the figure denote the regions where  
511    changes are statistically significant at the 0.1 level. Although SRE is largest over the  
512    mountains, surface air temperature change is largest around the mountains, such as  
513    over the Eastern Snake River Plain, Northern Utah, and Central-Southwestern  
514    Wyoming, where surface air temperatures are increased by around  $0.5\text{--}2^\circ\text{C}$  due to the  
515    aerosol SDE. The large surface air temperature increase corresponds well to the  
516    significant reductions of snow water equivalent (by 2–50 mm) and snow cover  
517    fraction (by 5–20%) in these regions. This indicates a pronounced positive feedback  
518    between snow albedo, radiation, and surface temperature around the mountains,  
519    where snow water equivalent values are relatively lower and snow cover fractions are  
520    smaller than those over the mountains. The positive feedback amplifies the surface  
521    warming and snow melting, as was also found in a previous study using the Weather  
522    Research and Forecasting (WRF) model (Qian et al., 2009). We note, however, both  
523    snow water equivalent and snow cover fraction are larger over the mountains. For



524 example, winter and spring snow cover fraction is mostly above 70% on the high  
525 mountains (see Figure 7 of Wu et al. (2017)). This suggests that snow on the high  
526 mountains is less susceptible to the aerosol SDE. Another reason for the smaller  
527 change of surface air temperature over the mountains is that snow water equivalent  
528 and snow cover fraction are increased (especially in the Northern Rockies and Greater  
529 Yellowstone region) due to the increase of snowfall in these regions (Figure 9f),  
530 which cancels out the reduction of snow water equivalent resulting from aerosol SDE.  
531 The increase of snowfall is due to enhanced water vapor transport from the Pacific  
532 Ocean (Figure not shown), which is likely related to the large-scale circulation change  
533 due to aerosol SDE. Note that increases of snow water equivalent and snow cover  
534 fraction in the Northern Rockies and Greater Yellowstone region due to aerosol SDE  
535 do not pass the significant test at 0.1 level because of the large interannual variability  
536 in these regions.

537 Table 2 gives the winter and spring surface air temperature changes due to  
538 LAAs in snow averaged over the five regions. Seasonal mean surface air temperature  
539 change is around 0.9-1.1 °C in the Eastern Snake River Plain in winter and spring,  
540 while this change is around 0.003-0.17 °C (winter) and around 0.3-0.5 °C (spring) in  
541 the mountainous regions (Northern Rockies, Greater Yellowstone region, and  
542 Southern Rockies). In Table 2, we also show the efficacy of snow albedo forcing,  
543 which is defined as the ratio of surface air temperature change to SRE. The efficacy is  
544 mostly around 0.1-0.5 in the three mountainous regions, but it is 1.3-2.2 in the Eastern



Snake River Plain and Southwestern Wyoming. This indicates that stronger snow albedo feedbacks exist in the latter two regions.

Figures 10-11 show the monthly evolution of regional mean surface air temperature, snow water equivalent, and snow cover fraction, and their changes due to aerosol SDE in the Eastern Snake River Plain and Southwestern Wyoming, respectively. Monthly variations of surface air temperature, snow water equivalent, and snow cover fraction are similar between the two regions: lowest surface air temperature and largest snow cover fraction in January, and highest snow water equivalent in February-March. Significant changes of these variables from the aerosol SDE occur in both regions. The largest surface air temperature increase is 1.5 °C in the Eastern Snake River Plain and 1.6 °C in Southwestern Wyoming, occurring in April and December, respectively. In the Eastern Snake River Plain (Southwestern Wyoming), aerosol SDE leads to the reduction of snow water equivalent by 6-28 mm (6-16 mm) and snow cover fraction by 5-15% (6-19%) from December to March, which corresponds to a fraction of 18-33% (20-37%) and 7-28% (8-28%), respectively, with respect to the NoSDE simulation results. In April (late snowmelt period) when snow water equivalent and snow cover fraction are both relatively small, the aerosol SDE is more significant, which reduces snow water equivalent values and snow cover fractions by about half.

#### 4.5 Runoff change induced by aerosol SDE



565           In the model, the runoff includes the surface runoff and sub-surface runoff.  
566   Runoff is mainly from the rainfall and snowmelt. The change of rainfall is shown in  
567   Figures 9c-9d, and the snowmelt change is shown in Figure 12. Aerosol SDE  
568   increases the snowmelt by 0.1-2 mm/day in the mountains during the snow  
569   accumulation and early snowmelt period (in autumn, winter and spring). In the late  
570   snowmelt period, aerosol SDE reduces the snowmelt due to less snowpack available  
571   for melting in the plains (in spring) and in the mountains (in summer). Note that  
572   snowmelt is slightly reduced by the aerosol SDE in autumn in the Southern Rockies,  
573   which is a result of less snowpack for melting due to the reduced snowfall in this  
574   region (Figure not shown).

575           Because of the change in rainfall and snowmelt due to aerosol SDE, surface  
576   runoff changes too. Figure 13 shows the runoff change induced by aerosol SDE in  
577   four seasons. In winter, runoff is barely modified by the aerosol SDE in the Rocky  
578   Mountains, except in the Northern Rockies where runoff is increased by 0.1-2 mm  
579   day<sup>-1</sup>, associated with increased rainfall (Figure 9c) and increased snowmelt (Figure  
580   12a). In spring, runoff changes the most compared to all of the other seasons, with the  
581   runoff increased by up to 0.5-2 mm day<sup>-1</sup> in the mountainous regions. This is mainly  
582   due to the increase of snowmelt resulting from surface warming (Figure 12b) as well  
583   as due to more snow available for melt resulting from snowfall increase (Figure 9f).  
584   The changes in runoff are statistically significant at 0.1 level in most of the  
585   mountainous regions in spring. Absolute runoff increases are stronger in the Northern



586 Rockies and Greater Yellowstone regions than in the Southern Rockies in terms of the  
587 area and magnitude, probably due to the smaller snow water equivalent in Southern  
588 Rockies (Wu et al., 2017). As more snowmelt occurs in spring, less snowpack is  
589 available for melt in summer and thus surface runoff is reduced by about 0.1-1 mm  
590 day<sup>-1</sup>. There is little runoff change in autumn, as there is less runoff generated from  
591 rainfall and snowmelt than in other seasons. Overall, BC and dust residing in snow  
592 accelerate the hydrologic cycles by increasing the runoff in spring and reducing the  
593 runoff in summer. Surface warming also increases the ratio of rainfall to total  
594 precipitation, which can accelerate the generation of runoff. Note that in some regions  
595 of the plains, such as the central-eastern Montana, Southwestern Wyoming, and Snake  
596 River Basin, the snowmelt changes by 0.1-1 mm/day due to the aerosol SDE, but the  
597 runoff changes little. This is because the water generated from snowmelt is mainly  
598 stored in soil or transformed into evapotranspiration in these regions. Also note that  
599 there are statistically significant increases of runoff in the southern Great Plains in  
600 spring, but the change is small (around 0.05-0.1 mm/day; Figure 13b). This change is  
601 a result of slight increases in both rainfall (Figure 9d) and snowmelt (Figure 12b).

602       Figure 14 shows the monthly evolution of runoff and its change due to the  
603 aerosol SDE in the three mountainous regions (Northern Rockies, Greater  
604 Yellowstone region, and Southern Rockies). In the three regions, runoff peaks in the  
605 late spring and early summer (in May in Northern Rockies and Southern Rockies, and  
606 in June in Greater Yellowstone region) when snow melting progresses after the peak



607 of snow water equivalent in early-to-middle April (Wu et al., 2017). This indicates the  
608 significant contribution of snowmelt to runoff. Overall, runoff changes are larger in  
609 the Northern Rockies and Greater Yellowstone region than in Southern Rockies,  
610 which is consistent with the spatial distribution of runoff changes shown in Figure 13.  
611 Runoff is significantly increased in spring and decreased in June and July, indicating  
612 the acceleration of the local hydrologic cycle by aerosol SDE. In the Northern  
613 Rockies, runoff is also increased from October to March but in much smaller  
614 magnitudes (below  $0.2 \text{ mm day}^{-1}$ ) compared to April and May. In April (May), runoff  
615 is increased by 0.39 (0.56), 0.22 (1.00), and 0.17 (0.15)  $\text{mm day}^{-1}$  in the the Northern  
616 Rockies, Greater Yellowstone region, and Southern Rockies, respectively. This  
617 increase contributes to 26% (13%), 42% (27%), and 29% (7%) of the runoff from the  
618 NoSDE simulation in April (May) for the three regions, respectively. The reduction of  
619 runoff in June is relatively small (0.06 and 0.11  $\text{mm day}^{-1}$ , respectively) in the  
620 Northern Rockies and Greater Yellowstone, only accounting for 2% of runoff from  
621 the NoSDE simulation. However, it reaches up to 0.18  $\text{mm day}^{-1}$  in the the Southern  
622 Rockies, which accounts for 15% of runoff. In addition, due to the reduction of snow  
623 available for melting in later month (i.e., July), the runoff is further reduced. With  
624 respect to the relative smaller runoff in July than in previous months, aerosol SDE is  
625 more significant, which can reduce the runoff by 0.04 (8%), 0.17 (23%), and 0.06  $\text{mm}$   
626  $\text{day}^{-1}$  (16%) in the three regions, respectively. Note that due to increase of



precipitation, the annual mean runoff is increased by 0.12 (12%), 0.09 (10%), and 0.01 mm day<sup>-1</sup> (2%) in these three regions, respectively.

## 5. Conclusions

In this study, we use VR-CESM to quantify the impacts of LAAs (BC and dust) deposition on the snowpack and hydrologic cycles in the Rocky Mountains. Our previous study has shown that VR-CESM reproduces reasonably the spatial distributions and seasonal evolution of snowpack in the Rocky Mountains (Wu et al., 2017). Here we show that the model also reproduces observed spatial distributions of near-surface BC and dust concentrations in the western U.S. compared to IMPROVE observations. The magnitude of simulated near-surface dust concentrations is comparable to observations, while that of simulated near-surface BC concentrations is mostly underestimated, especially in the Rocky Mountain region. The underestimation of near-surface BC concentrations may be due to the absence of local sources for BC emissions used in the model. Simulated aerosol-in-snow concentrations are closely related to the distributions of both snowpack and near-surface atmospheric aerosol concentrations. Simulated BC-in-snow concentrations are mostly comparable to the observations with the magnitude between 2 and 30 ng g<sup>-1</sup>, although significant underestimations (by as much as a factor of 10) were found at two stations.

Due to the deposition of LAAs on snow cover, surface net shortwave radiation is increased. Regional averaged SRE induced by LAAs in snow is 0.1-0.5 W m<sup>-2</sup> in



648 winter in the three mountainous regions (Northern Rockies, Greater Yellowstone  
649 region, and Southern Rockies) and  $0.4\text{--}0.6\text{ W m}^{-2}$  in the two regions around the  
650 mountains (Eastern Snake River Plain and Southwestern Wyoming). SRE is much  
651 larger in spring and reaches up to  $0.6\text{--}1.7\text{ W m}^{-2}$  in these five regions (Table 2). Dust  
652 contributes 21–43% to the total SRE induced by LAAs in snow in spring, indicating  
653 the important role of dust residing in snow. Of the five regions, dust contributes the  
654 most (43%) to the total SRE in the Southern Rockies. This is not unexpected as this  
655 region is close to dust sources in the Colorado Plateau.

656 As a result of SRE induced by LAAs in snow, surface air temperature  
657 increases in most of the Rocky Mountain region. The surface air temperature increase  
658 is largest over the Eastern Snake River Plain and Southwestern Wyoming, with winter  
659 and spring surface air temperature increased by  $0.9\text{--}1.1^{\circ}\text{C}$ . Significant reductions of  
660 snow water equivalent (by 2–50 mm) and snow cover fraction (by 5–20%) occur in  
661 these two regions, indicating a strong positive snow-albedo feedback there.

662 Aerosol SDE accelerates the hydrologic cycle in the mountainous regions. In  
663 April and May, monthly mean runoff is increased by 7%–42% in the three  
664 mountainous regions (Northern Rockies, Greater Yellowstone region, Southern  
665 Rockies). This is because of the accelerated snowmelt resulting from surface warming  
666 as well as the increased snowfall resulting from enhanced water vapor transport from  
667 the Pacific Ocean. The enhanced water vapor transport may be related to large-scale  
668 circulation changes. In the later stage of snowmelt, monthly runoff is reduced by 2–15%





669 in June and 8-23% in July in the three mountainous regions. In particular, aerosol  
670 SDE leads to a reduction of total runoff by about 15% in June and July in the  
671 Southern Rockies. This highlights the important role of aerosol SDE in modulating  
672 the hydrologic cycle in the mountainous regions.

673 We note that VR-CESM still underestimates the near-surface BC  
674 concentrations, however, reproduces observed magnitudes of BC-in-snow  
675 concentrations for most stations. For dust in snow, the model used in this study only  
676 accounts for dust particles smaller than 10  $\mu\text{m}$ , while observations made by Reynolds  
677 et al. (2016) suggest that most airborne dust concentrations are characterized by dust  
678 particles with diameters larger than 10  $\mu\text{m}$  in the Utah-Colorado region. Therefore,  
679 our simulations may significantly underestimate the impacts of dust in snow. Actually,  
680 our simulations suggest SRE induced by dust-in-snow can reach up to 2-5  $\text{W m}^{-2}$  in  
681 the Southern Rockies, which is nearly an order of magnitude smaller than values in  
682 Painter et al. (2007) based on observed dust-in-snow particles. Future observations of  
683 LAAs in snow, particularly for the temporal evolution of LAAs in different snow  
684 layers, as well as detailed size distribution measurements of dust particles in snow  
685 will help reduce the uncertainties in the model quantification of the impacts of LAAs  
686 in snow.

687 Although the uncertainties still exist, our results show LAAs in snow can  
688 significantly affect the snowpack and consequent hydrologic cycle in the Rocky  
689 Mountains. Previous studies have demonstrated that snowpack on the Rocky



Mountains has declined significantly in the second half of 20th century (e.g.,  
Pederson et al., 2011). The role of LAAs in this decrease of snowpack is still  
unknown. It would be interesting to investigate the role of LAAs and compare it with  
those of other climate factors (such as natural climate variability and greenhouse gas  
concentrations). Moreover, BC and dust emissions may also be subject to changes in  
the future. Therefore, for better projections of future changes in Rocky Mountain  
snowpack, the impacts of LAAs in snow under future emissions scenarios also need to  
be taken into account.

698

#### 699 **Acknowledgement**

This research is supported by the University of Wyoming Tier-1 Engineering  
Initiative for High-Performance Computational Science and Technology funded by  
the State of Wyoming. Z. Lin was jointly supported by the Special Scientific Research  
Fund of the Meteorological Public Welfare Profession of China (grant  
GYHY01406021), National Key Research and Development Program of China (grant  
2016YFC0402702), and the National Natural Science Foundation of China (grant  
41575095). We thank the team for maintaining the Interagency Monitoring of  
PROtected Visual Environments (IMPROVE) network and making the observation  
dataset available to use (<http://vista.cira.colostate.edu/Improve/improve-data/>). We  
also thank Dr. Sarah Doherty from the University of Washington and Dr. S.  
McKenzie Skiles from Jet Propulsion Laboratory, California Institute of Technology



711 for providing the observations of absorbing aerosols in snow and helpful suggestions  
712 on use of the data. We thank Alan M. Rhoades and Paul A. Ullrich from University of  
713 California, Davis as well as Colin M. Zarzycki from NCAR for helpful discussions  
714 during this study. We would like to acknowledge the use of computational resources  
715 by conducting the model simulations (ark:/85065/d7wd3xhc) at the NCAR-Wyoming  
716 Supercomputing Center provided by the NSF and the State of Wyoming, and  
717 supported by NCAR's Computational and Information Systems Laboratory. The  
718 simulation results can be obtained by contacting the corresponding author X. Liu  
719 ([xliu6@uwyo.edu](mailto:xliu6@uwyo.edu)).

720

## 721 **References**

- 722 Abatzoglou, J. T.: Influence of the PNA on declining mountain snowpack in the  
723 Western United States, *International Journal of Climatology*, 31, 1135-1142,  
724 10.1002/joc.2137, 2011.
- 725 Andreae, M. O., and Gelencsér, A.: Black carbon or brown carbon? The nature of  
726 light-absorbing carbonaceous aerosols, *Atmos. Chem. Phys.*, 6, 3131-3148,  
727 10.5194/acp-6-3131-2006, 2006.
- 728 Dennis, J. M., Edwards, J., Evans, K. J., Guba, O., Lauritzen, P. H., Mirin, A. A.,  
729 St-Cyr, A., Taylor, M. A., and Worley, P. H.: CAM-SE: A scalable spectral  
730 element dynamical core for the Community Atmosphere Model, *The*  
731 *International Journal of High Performance Computing Applications*, 26, 74-89,  
732 doi:10.1177/1094342011428142, 2012.
- 733 Doherty, S. J., Dang, C., Hegg, D. A., Zhang, R., and Warren, S. G.: Black carbon  
734 and other light-absorbing particles in snow of central North America, *Journal of*  
735 *Geophysical Research: Atmospheres*, 119, 12,807-812,831,  
736 10.1002/2014JD022350, 2014.
- 737 Doherty, S. J., Hegg, D. A., Johnson, J. E., Quinn, P. K., Schwarz, J. P., Dang, C., and



- 738 Warren, S. G.: Causes of variability in light absorption by particles in snow at  
739 sites in Idaho and Utah, *Journal of Geophysical Research: Atmospheres*, 121,  
740 2015JD024375, 10.1002/2015JD024375, 2016.
- 741 Flanner, M. G., Zender, C. S., Randerson, J. T., and Rasch, P. J.: Present-day climate  
742 forcing and response from black carbon in snow, *Journal of Geophysical*  
743 *Research: Atmospheres*, 112, D11202, 10.1029/2006JD008003, 2007.
- 744 Flanner, M. G., Zender, C. S., Hess, P. G., Mahowald, N. M., Painter, T. H.,  
745 Ramanathan, V., and Rasch, P. J.: Springtime warming and reduced snow cover  
746 from carbonaceous particles, *Atmos. Chem. Phys.*, 9, 2481-2497,  
747 10.5194/acp-9-2481-2009, 2009.
- 748 Flanner, M. G., Liu, X., Zhou, C., Penner, J. E., and Jiao, C.: Enhanced solar energy  
749 absorption by internally-mixed black carbon in snow grains, *Atmos. Chem. Phys.*,  
750 12, 4699-4721, 10.5194/acp-12-4699-2012, 2012.
- 751 Gates, W. L.: AMIP: The Atmospheric Model Intercomparison Project, *Bulletin of*  
752 *the American Meteorological Society*, 73, 1962-1970,  
753 10.1175/1520-0477(1992)073<1962:atamip>2.0.co;2, 1992.
- 754 Ginoux, P., Prospero, J. M., Gill, T. E., Hsu, N. C., and Zhao, M.: Global-Scale  
755 Attribution of Anthropogenic and Natural Dust Sources and Their Emission  
756 Rates Based on Modis Deep Blue Aerosol Products, *Rev Geophys*, 50, Artn  
757 Rg3005, doi 10.1029/2012rg000388, 2012.
- 758 Haarsma, R. J., Roberts, M. J., Vidale, P. L., Senior, C. A., Bellucci, A., Bao, Q.,  
759 Chang, P., Corti, S., Fučkar, N. S., Guemas, V., von Hardenberg, J., Hazeleger,  
760 W., Kodama, C., Koenig, T., Leung, L. R., Lu, J., Luo, J. J., Mao, J.,  
761 Mizielinski, M. S., Mizuta, R., Nobre, P., Satoh, M., Scoccimarro, E., Semmler,  
762 T., Small, J., and von Storch, J. S.: High Resolution Model Intercomparison  
763 Project (HighResMIP v1.0) for CMIP6, *Geosci. Model Dev.*, 9, 4185-4208,  
764 10.5194/gmd-9-4185-2016, 2016.
- 765 Hansen, J., and Nazarenko, L.: Soot climate forcing via snow and ice albedos,  
766 *Proceedings of the National Academy of Sciences of the United States of*  
767 *America*, 101, 423-428, 10.1073/pnas.2237157100, 2004.
- 768 Huang, X., Rhoades, A. M., Ullrich, P. A., and Zarzycki, C. M.: An evaluation of the  
769 variable-resolution CESM for modeling California's climate, *Journal of*  
770 *Advances in Modeling Earth Systems*, 8, 345-369, 10.1002/2015MS000559,  
771 2016.



- 772 Hurrell, J. W., Hack, J. J., Shea, D., Caron, J. M., and Rosinski, J.: A New Sea  
773 Surface Temperature and Sea Ice Boundary Dataset for the Community  
774 Atmosphere Model, *J Climate*, 21, 5145-5153, 10.1175/2008jcli2292.1, 2008.
- 775 Hurrell, J. W., Holland, M. M., Gent, P. R., Ghan, S., Kay, J. E., Kushner, P. J.,  
776 Lamarque, J. F., Large, W. G., Lawrence, D., Lindsay, K., Lipscomb, W. H.,  
777 Long, M. C., Mahowald, N., Marsh, D. R., Neale, R. B., Rasch, P., Vavrus, S.,  
778 Vertenstein, M., Bader, D., Collins, W. D., Hack, J. J., Kiehl, J., and Marshall, S.:  
779 The Community Earth System Model: A Framework for Collaborative Research,  
780 *Bulletin of the American Meteorological Society*, 94, 1339-1360,  
781 10.1175/BAMS-D-12-00121.1, 2013.
- 782 Iacono, M. J., Delamere, J. S., Mlawer, E. J., Shephard, M. W., Clough, S. A., and  
783 Collins, W. D.: Radiative forcing by long-lived greenhouse gases: Calculations  
784 with the AER radiative transfer models, *Journal of Geophysical Research:*  
785 *Atmospheres*, 113, D13103, 10.1029/2008JD009944, 2008.
- 786 Kavouras, I. G., Etyemezian, V., Xu, J., DuBois, D. W., Green, M., and Pitchford, M.:  
787 Assessment of the local windblown component of dust in the western United  
788 States, *Journal of Geophysical Research: Atmospheres*, 112, n/a-n/a,  
789 10.1029/2006JD007832, 2007.
- 790 Koch, D., Schulz, M., Kinne, S., McNaughton, C., Spackman, J. R., Balkanski, Y.,  
791 Bauer, S., Berntsen, T., Bond, T. C., Boucher, O., Chin, M., Clarke, A., De Luca,  
792 N., Dentener, F., Diehl, T., Dubovik, O., Easter, R., Fahey, D. W., Feichter, J.,  
793 Fillmore, D., Freitag, S., Ghan, S., Ginoux, P., Gong, S., Horowitz, L., Iversen,  
794 T., Kirkev, aring, g, A., Klimont, Z., Kondo, Y., Krol, M., Liu, X., Miller, R.,  
795 Montanaro, V., Moteki, N., Myhre, G., Penner, J. E., Perlwitz, J., Pitari, G.,  
796 Reddy, S., Sahu, L., Sakamoto, H., Schuster, G., Schwarz, J. P., Seland, Ø., Stier,  
797 P., Takegawa, N., Takemura, T., Textor, C., van Aardenne, J. A., and Zhao, Y.:  
798 Evaluation of black carbon estimations in global aerosol models, *Atmos. Chem.*  
799 *Phys.*, 9, 9001-9026, 10.5194/acp-9-9001-2009, 2009.
- 800 Lamarque, J. F., Bond, T. C., Eyring, V., Granier, C., Heil, A., Klimont, Z., Lee, D.,  
801 Liousse, C., Mieville, A., Owen, B., Schultz, M. G., Shindell, D., Smith, S. J.,  
802 Stehfest, E., Van Aardenne, J., Cooper, O. R., Kainuma, M., Mahowald, N.,  
803 McConnell, J. R., Naik, V., Riahi, K., and van Vuuren, D. P.: Historical  
804 (1850–2000) gridded anthropogenic and biomass burning emissions of reactive  
805 gases and aerosols: methodology and application, *Atmos. Chem. Phys.*, 10,



- 806 7017-7039, 10.5194/acp-10-7017-2010, 2010.
- 807 Lauritzen, P. H., Bacmeister, J. T., Callaghan, P. F., and Taylor, M. A.: NCAR\_Topo  
808 (v1.0): NCAR global model topography generation software for unstructured  
809 grids, *Geosci. Model Dev.*, 8, 3975-3986, 10.5194/gmd-8-3975-2015, 2015.
- 810 Liu, X., Easter, R. C., Ghan, S. J., Zaveri, R., Rasch, P., Shi, X., Lamarque, J. F.,  
811 Gettelman, A., Morrison, H., Vitt, F., Conley, A., Park, S., Neale, R., Hannay, C.,  
812 Ekman, A. M. L., Hess, P., Mahowald, N., Collins, W., Iacono, M. J., Bretherton,  
813 C. S., Flanner, M. G., and Mitchell, D.: Toward a minimal representation of  
814 aerosols in climate models: description and evaluation in the Community  
815 Atmosphere Model CAM5, *Geosci. Model Dev.*, 5, 709-739,  
816 10.5194/gmd-5-709-2012, 2012.
- 817 Malm, W. C., Sisler, J. F., Huffman, D., Eldred, R. A., and Cahill, T. A.: Spatial and  
818 seasonal trends in particle concentration and optical extinction in the United  
819 States, *Journal of Geophysical Research: Atmospheres*, 99, 1347-1370,  
820 10.1029/93JD02916, 1994.
- 821 Malm, W. C., Pitchford, M. L., McDade, C., and Ashbaugh, L. L.: Coarse particle  
822 speciation at selected locations in the rural continental United States, *Atmos*  
823 *Environ*, 41, 2225-2239, <http://doi.org/10.1016/j.atmosenv.2006.10.077>, 2007.
- 824 Morrison, H., and Gettelman, A.: A New Two-Moment Bulk Stratiform Cloud  
825 Microphysics Scheme in the Community Atmosphere Model, Version 3 (CAM3).  
826 Part I: Description and Numerical Tests, *J Climate*, 21, 3642-3659,  
827 10.1175/2008JCLI2105.1, 2008.
- 828 Neale, R. B., and Coauthors: Description of the NCAR Community Atmosphere  
829 Model (CAM5). *NCAR Tech. Note. NCAR/TN-485+STR*, Natl. Cent. for Atmos.  
830 Res., Boulder, CO, 2010.
- 831 Oaida, C. M., Xue, Y., Flanner, M. G., Skiles, S. M., De Sales, F., and Painter, T. H.:  
832 Improving snow albedo processes in WRF/SSiB regional climate model to assess  
833 impact of dust and black carbon in snow on surface energy balance and  
834 hydrology over western U.S, *Journal of Geophysical Research: Atmospheres*,  
835 120, 3228-3248, 10.1002/2014JD022444, 2015.
- 836 Oleson, K. W., D. M. Lawrence, B. Gordon, M. G. Flanner, E. Kluzek, J. Peter, S.  
837 Levis, S. C. Swenson, E. Thornton, and J. Feddema: Technical description of  
838 version 4.0 of the Community Land Model (CLM), *NCAR Tech. Note*  
839 *NCAR/TN-4781STR*, Natl. Cent. for Atmos. Res., Boulder, CO, 2010.



- 840 Painter, T. H., Barrett, A. P., Landry, C. C., Neff, J. C., Cassidy, M. P., Lawrence, C.  
841 R., McBride, K. E., and Farmer, G. L.: Impact of disturbed desert soils on  
842 duration of mountain snow cover, *Geophys Res Lett*, 34, n/a-n/a,  
843 10.1029/2007GL030284, 2007.
- 844 Painter, T. H., Deems, J. S., Belnap, J., Hamlet, A. F., Landry, C. C., and Udall, B.:  
845 Response of Colorado River runoff to dust radiative forcing in snow,  
846 *Proceedings of the National Academy of Sciences*, 107, 17125-17130,  
847 10.1073/pnas.0913139107, 2010.
- 848 Painter, T. H., Skiles, S. M., Deems, J. S., Bryant, A. C., and Landry, C. C.: Dust  
849 radiative forcing in snow of the Upper Colorado River Basin: 1. A 6 year record  
850 of energy balance, radiation, and dust concentrations, *Water Resources Research*,  
851 48, W07521, 10.1029/2012WR011985, 2012.
- 852 Park, S., and Bretherton, C. S.: The University of Washington Shallow Convection  
853 and Moist Turbulence Schemes and Their Impact on Climate Simulations with  
854 the Community Atmosphere Model, *J Climate*, 22, 3449-3469,  
855 10.1175/2008JCLI2557.1, 2009.
- 856 Park, S., Bretherton, C. S., and Rasch, P. J.: Integrating Cloud Processes in the  
857 Community Atmosphere Model, Version 5, *J Climate*, 27, 6821-6856,  
858 10.1175/JCLI-D-14-00087.1, 2014.
- 859 Pederson, G. T., Gray, S. T., Woodhouse, C. A., Betancourt, J. L., Fagre, D. B., Littell,  
860 J. S., Watson, E., Luckman, B. H., and Graumlich, L. J.: The Unusual Nature of  
861 Recent Snowpack Declines in the North American Cordillera, *Science*, 333,  
862 332-335, 10.1126/science.1201570, 2011.
- 863 Qian, Y., Gustafson, W. I., Leung, L. R., and Ghan, S. J.: Effects of soot-induced  
864 snow albedo change on snowpack and hydrological cycle in western United  
865 States based on Weather Research and Forecasting chemistry and regional  
866 climate simulations, *Journal of Geophysical Research: Atmospheres*, 114, n/a-n/a,  
867 10.1029/2008JD011039, 2009.
- 868 Qian, Y., Flanner, M. G., Leung, L. R., and Wang, W.: Sensitivity studies on the  
869 impacts of Tibetan Plateau snowpack pollution on the Asian hydrological cycle  
870 and monsoon climate, *Atmos. Chem. Phys.*, 11, 1929-1948,  
871 10.5194/acp-11-1929-2011, 2011.
- 872 Qian, Y., Wang, H., Zhang, R., Flanner, M. G., and Rasch, P. J.: A sensitivity study  
873 on modeling black carbon in snow and its radiative forcing over the Arctic and



- 874 Northern China, Environmental Research Letters, 9, 064001, 2014.
- 875 Qian, Y., Yasunari, T. J. , Doherty, S. J., Flanner, M. G., Lau, W. K. M., Ming, J.,
- 876 Wang, H., Wang, M., Warren, S. G., Zhang, R.: Light-absorbing Particles in
- 877 Snow and Ice: Measurement and Modeling of Climatic and Hydrological impact,
- 878 Adv. Atmos. Sci., 32, 64-91, 10.1007/s00376-014-0010-0, 2015.
- 879 Reynolds, R. L., Munson, S. M., Fernandez, D., Goldstein, H. L., and Neff, J. C.:
- 880 Concentrations of mineral aerosol from desert to plains across the central Rocky
- 881 Mountains, western United States, Aeolian Res, 23, 21-35,
- 882 <http://doi.org/10.1016/j.aeolia.2016.09.001>, 2016.
- 883 Rhoades, A. M., Huang, X., Ullrich, P. A., and Zarzycki, C. M.: Characterizing Sierra
- 884 Nevada Snowpack Using Variable-Resolution CESM, Journal of Applied
- 885 Meteorology and Climatology, 55, 173-196, 10.1175/jamc-d-15-0156.1, 2016.
- 886 Rhoades, A. M., Ullrich, P. A., and Zarzycki, C. M.: Projecting 21st century
- 887 snowpack trends in western USA mountains using variable-resolution CESM,
- 888 Climate Dynamics, 1-28, doi:10.1007/s00382-017-3606-0, 2017.
- 889 Richter, J. H., and Rasch, P. J.: Effects of Convective Momentum Transport on the
- 890 Atmospheric Circulation in the Community Atmosphere Model, Version 3, J
- 891 Climate, 21, 1487-1499, 10.1175/2007JCLI1789.1, 2008.
- 892 Sakaguchi, K., Leung, L. R., Zhao, C., Yang, Q., Lu, J., Hagos, S., Rauscher, S. A.,
- 893 Dong, L., Ringler, T. D., and Lauritzen, P. H.: Exploring a Multiresolution
- 894 Approach Using AMIP Simulations, J Climate, 28, 5549-5574,
- 895 10.1175/jcli-d-14-00729.1, 2015.
- 896 Serreze, M. C., Clark, M. P., Armstrong, R. L., McGinnis, D. A., and Pulwarty, R. S.:
- 897 Characteristics of the western United States snowpack from snowpack telemetry
- 898 (SNOTEL) data, Water Resources Research, 35, 2145-2160,
- 899 10.1029/1999WR900090, 1999.
- 900 Skiles S. M. and Painter T. H.: A 9-yr record of dust on snow in the Colorado River
- 901 Basin. 12th Biennial Conference of Science and Management on the Colorado
- 902 Plateau, 3-11, 2016a.
- 903 Skiles, S. M., and Painter, T.: Daily evolution in dust and black carbon content, snow
- 904 grain size, and snow albedo during snowmelt, Rocky Mountains, Colorado,
- 905 Journal of Glaciology, 63, 118-132, 10.1017/jog.2016.125, 2016b.
- 906 Toon, O. B., McKay, C. P., Ackerman, T. P., and Santhanam, K.: Rapid calculation of
- 907 radiative heating rates and photodissociation rates in inhomogeneous multiple





- 908 scattering atmospheres, *Journal of Geophysical Research: Atmospheres*, 94,  
909 16287-16301, 10.1029/JD094iD13p16287, 1989.
- 910 Ullrich, P. A.: SQuadGen: Spherical quadrilateral grid generator. University of  
911 California, Davis, Climate and Global Change Group software, available online  
912 at <https://github.com/ClimateGlobalChange/squadgen> (last access: 24 April  
913 2017), 2014.
- 914 Warren, S. G., and Wiscombe, W. J.: A Model for the Spectral Albedo of Snow. II:  
915 Snow Containing Atmospheric Aerosols, *J Atmos Sci*, 37, 2734-2745,  
916 10.1175/1520-0469(1980)037<2734:amftsa>2.0.co;2, 1980.
- 917 Wells, K. C., Witek, M., Flatau, P., Kreidenweis, S. M., and Westphal, D. L.: An  
918 analysis of seasonal surface dust aerosol concentrations in the western US  
919 (2001–2004): Observations and model predictions, *Atmos Environ*, 41,  
920 6585-6597, <http://doi.org/10.1016/j.atmosenv.2007.04.034>, 2007.
- 921 Wu, C., Lin, Z., He, J., Zhang, M., Liu, X., Zhang, R., and Brown, H.: A  
922 process-oriented evaluation of dust emission parameterizations in CESM:  
923 Simulation of a typical severe dust storm in East Asia, *Journal of Advances in*  
924 *Modeling Earth Systems*, 8, 1432-1452, 10.1002/2016MS000723, 2016.
- 925 Wu, C., X. Liu, Z. Lin, A. M. Rhoades, P. A. Ullrich, C. M. Zarzycki, Z. Lu, and S.  
926 R. Rahimi-Esfarjani: Exploring a variable-resolution approach for simulating  
927 regional climate in the Rocky Mountain region using the VR-CESM, submitted  
928 to *Journal of Geophysical Research: Atmospheres*, 2017.
- 929 Yasunari, T. J., Koster, R. D., Lau, W. K. M., and Kim, K.-M.: Impact of snow  
930 darkening via dust, black carbon, and organic carbon on boreal spring climate in  
931 the Earth system, *Journal of Geophysical Research: Atmospheres*, 120,  
932 2014JD022977, 10.1002/2014JD022977, 2015.
- 933 Zarzycki, C. M., and Jablonowski, C.: A multidecadal simulation of Atlantic tropical  
934 cyclones using a variable-resolution global atmospheric general circulation  
935 model, *Journal of Advances in Modeling Earth Systems*, 6, 805-828,  
936 10.1002/2014MS000352, 2014.
- 937 Zarzycki, C. M., Jablonowski, C., and Taylor, M. A.: Using Variable-Resolution  
938 Meshes to Model Tropical Cyclones in the Community Atmosphere Model, *Mon*  
939 *Weather Rev*, 142, 1221-1239, 10.1175/mwr-d-13-00179.1, 2014a.
- 940 Zarzycki, C. M., Levy, M. N., Jablonowski, C., Overfelt, J. R., Taylor, M. A., and  
941 Ullrich, P. A.: Aquaplanet Experiments Using CAM's Variable-Resolution



942         Dynamical Core, J Climate, 27, 5481-5503, 10.1175/jcli-d-14-00004.1, 2014b.  
943         Zarzycki, C. M., Jablonowski, C., Thatcher, D. R., and Taylor, M. A.: Effects of  
944         Localized Grid Refinement on the General Circulation and Climatology in the  
945         Community Atmosphere Model, J Climate, 28, 2777-2803,  
946         10.1175/jcli-d-14-00599.1, 2015.  
947         Zhang, G. J., and McFarlane, N. A.: Sensitivity of climate simulations to the  
948         parameterization of cumulus convection in the Canadian Climate Centre general  
949         circulation model, Atmosphere-Ocean, 33, 407-446, 1995.  
950         Zhang, R., Wang, H., Hegg, D. A., Qian, Y., Doherty, S. J., Dang, C., Ma, P. L.,  
951         Rasch, P. J., and Fu, Q.: Quantifying sources of black carbon in western North  
952         America using observationally based analysis and an emission tagging technique  
953         in the Community Atmosphere Model, Atmos. Chem. Phys., 15, 12805-12822,  
954         10.5194/acp-15-12805-2015, 2015.  
955  
956



**Table 1.** Observations of BC mass concentration in snow column ( $C_{BC}$ ,  $\text{ng g}^{-1}$ , i.e., ng gram BC per g snow) in the Rocky Mountain region compiled from previously published literature.

No.	Latitude (°N)	Longitude (°W)	Elevation (m)	Date sampled	$C_{BC}$ ( $\text{ng g}^{-1}$ ) <sup>a</sup>	Source
1	40.9014	115.8910	1949	2/1/13	7.6	Site 8 of Doherty et al. (2014)
2	42.2767	116.0115	1772	2/1/13	5.6	Site 9 of Doherty et al. (2014)
3	43.3495	115.3968	1538	2/3/13	6.0	Site 10 of Doherty et al. (2014)
4	43.5927	113.5894	1942	2/3/13	5.8	Site 11 of Doherty et al. (2014)
5	43.4010	111.2053	1727	2/4/13	6.8	Site 12 of Doherty et al. (2014)
6	42.9357	109.8576	2274	2/4/13	6.3	Site 13 of Doherty et al. (2014)
7	41.7297	109.3668	2223	2/5/13	29.1	Site 14 of Doherty et al. (2014)
8	40.7464	109.4776	2583	2/5/13	9.3	Site 15 of Doherty et al. (2014)
9	40.1316	109.4711	1538	2/7/13	14.3	Site 16 of Doherty et al. (2014)
10	40.4929	107.8994	1962	2/8/13	9.5	Site 17 of Doherty et al. (2014)
11	40.6695	106.4158	2512	2/9/13	11.4	Site 18 of Doherty et al. (2014)
12	48.2318	105.0949	648	2/17/13	10.9	Site 24 of Doherty et al. (2014)
13	44.9475	116.0813	1528	January to March, 2014	9.8 (5.4)	Site McCall of Doherty et al. (2016)
14	44.4224	115.9899	1450	February to March, 2014	13.3 (9.5)	Site Cascade Valley of Doherty et al. (2016)
15	44.0949	115.9771	960	February to March, 2014	14.9 (8.9)	Site Garden Valley of Doherty et al. (2016)
16	40.143	109.467	1620	February to March, 2013 and 2014	33.6 (25.4)	Site Vernal of Doherty et al. (2016)
17	37.9069	107.7113	3368	March to May, 2013	9.1 (7.9)	At Senator Beck Basin Study Area (SBBSA) (Skiles and Painter, 2016b)

<sup>a</sup>: If multi-measurements of  $C_{BC}$  are made during the observation period, the mean  $C_{BC}$  is given with the standard deviation of  $C_{BC}$  shown in parenthesis next to the mean  $C_{BC}$ .



964

965 **Table 2.** Winter (December-January-February) and spring (March-April-May) mean  
 966 surface shortwave radiative effect (SRE;  $\text{W m}^{-2}$ ) due to BC alone, dust alone and BC  
 967 and dust together in snow, as well as surface air temperature (SAT;  $^{\circ}\text{C}$ ) change and  
 968 the efficacy of SRE in SAT change in the five regions (see Figure 1c). Note that SRE  
 969 induced by BC and dust together is slightly larger than the sum of SRE induced by  
 970 BC and SRE by dust separately.

971

Season	SRE by BC <sup>a</sup>	SRE by dust <sup>a</sup>	SRE by BC & dust	SAT change	Efficacy <sup>b</sup>
Northern Rockies					
Winter	0.13 (92%)	0.01 (8%)	0.14	0.08	0.57
Spring	0.42 (79%)	0.11 (21%)	0.57	0.32	0.56
Greater Yellowstone region					
Winter	0.24 (88%)	0.03 (12%)	0.28	0.004	0.014
Spring	1.11 (71%)	0.45 (29%)	1.70	0.50	0.29
Southern Rockies					
Winter	0.36 (77%)	0.11 (23%)	0.50	0.17	0.34
Spring	0.79 (58%)	0.58 (42%)	1.58	0.30	0.19
Eastern Snake River Plain					
Winter	0.50 (84%)	0.09 (16%)	0.62	0.93	1.5
Spring	0.54 (73%)	0.20 (27%)	0.80	1.13	1.41
Southwestern Wyoming					
Winter	0.33 (81%)	0.08 (19%)	0.43	0.93	2.16
Spring	0.43 (67%)	0.22 (33%)	0.70	0.90	1.29

972 <sup>a</sup>: The fraction of SRE by BC (dust) to the sum of SRE by BC and SRE by dust is given in  
 973 parenthesis next to SRE by BC (dust).

974 <sup>b</sup>: Efficacy of snow/ice albedo forcing ( $^{\circ}\text{C}$  increase per  $1 \text{ W m}^{-2}$ ) is defined as the ratio of SAT  
 975 change to SRE.

976



977 **Figure captions:**

978

979 **Figure 1.** (a) Model meshes for variable resolution (uniform  $1^\circ$  with refined  $0.125^\circ$  in  
 980 the Rocky Mountains) used in VR-CESM. Note that each element shown contains  
 981 additional  $3 \times 3$  collocation gridcells. (b) Terrain height (m) in the western US with the  
 982 refined region at a resolution of  $0.125^\circ$  surrounded by dashed lines. (c) Five regions  
 983 identified for the analysis in this study, including three mountainous region (1,  
 984 Northern Rockies; 2, Greater Yellowstone region; 3, Southern Rockies) and two  
 985 regions in the plains around the mountains (4, Eastern Snake River Plain; 5,  
 986 Southwestern Wyoming).

987 **Figure 2.** Spatial distribution of cold season (winter and spring) mean (a) BC  
 988 emission flux and (b) near-surface BC concentration from the VR-CESM simulation;  
 989 (c) and (d) for dust emission flux and near-surface dust concentration, respectively.  
 990 Also shown are the IMPROVE stations (blue open circle) selected for model  
 991 validation, with the size of the circles from small to large indicating the magnitude of  
 992 observed near-surface BC/dust concentrations. The black rectangles in (b) and (d)  
 993 denotes the five regions (A, West Coast; B, Rocky Mountains; C, Utah and Nevada;  
 994 D, Southwestern US; E, Great Plain), which will be used to classify the stations in  
 995 Figure 3. Note that units for BC and dust concentrations are  $\text{ng m}^{-3}$  and  $\mu\text{g m}^{-3}$ ,  
 996 respectively.

997 **Figure 3.** Comparison of cold season mean near-surface (a) BC and (b) dust  
 998 concentrations at IMPROVE stations from VR-CESM simulation and IMPROVE  
 999 observations. Also given are the mean results at all the stations from simulation and  
 1000 observations and their correlation coefficient ( $R$ ). The 1:1 (solid) and 1:5/5:1 (dash)  
 1001 lines are plotted for reference.

1002 **Figure 4.** Winter (December-January-February (DJF); left) and spring  
 1003 (March-April-May (MAM); right) mean BC (upper row) and dust (bottom row) mass  
 1004 mixing ratios in snow column. Also shown are the stations for observations of BC  
 1005 mass in snow column (a, b) and for observations of dust mass in snow column at  
 1006 Senator Beck Basin Study Area (SBBBSA) in the San Juan Mountains (c, d). Note that  
 1007 the units for BC and dust mass mixing ratios are given in different units, i.e.,  $\text{ng g}^{-1}$   
 1008 and  $\mu\text{g g}^{-1}$ , respectively.

1009 **Figure 5.** Comparison of BC mass concentrations in the snow column ( $C_{\text{BC}}$ ) at the 17  
 1010 sites (see Table 1) from VR-CESM simulations and observations with the error bars



denoting the corresponding standard deviations. The observations are compiled from the previously published studies (Table 1). If multiple observations are recorded at a certain site, the observed standard deviations are calculated from these multiple observations (section 3). Simulated BC mass concentration in the snow column and its standard deviation are calculated from the 25-year mean and standard deviation of simulation in the same month as the observations (section 3).

**Figure 6.** Winter (December-January-February (DJF), left) and spring (March-April-May (MAM), right) mean surface shortwave radiative effect (SRE,  $\text{W m}^{-2}$ ) induced by BC (top) and dust (bottom).

**Figure 7.** Monthly variations of surface radiative effect (SRE;  $\text{W m}^{-2}$ ) during the water year (October 1st to September 30th) averaged over the Northern Rockies, Greater Yellowstone region, Southern Rockies, Eastern Snake River Basin, and Southwestern Wyoming, respectively.

**Figure 8.** Changes in surface air temperature (upper row;  $^{\circ}\text{C}$ ), snow water equivalent (bottom row; mm), and snow cover fraction (bottom row; %) in winter (left) and spring (right) induced by BC- and dust-in-snow. The crosses denote the regions where changes are statistically significant at 0.1 level.

**Figure 9.** As Figure 8, but for total precipitation change (top), rainfall change (center), and snowfall change (bottom). The unit is  $\text{mm day}^{-1}$ .

**Figure 10.** Seasonal evolution of (a) surface air temperature, (c) snow water equivalent, and (e) snow cover fraction and their changes due to SDE (b, d, and f) averaged over the Eastern Snake River Plain.

**Figure 11.** As Figure 10, but for Southwestern Wyoming.

**Figure 12.** Snowmelt change ( $\text{mm day}^{-1}$ ) due to SDE of BC and dust in four seasons: (a) December-January-February (DJF), (b) March-April-May (MAM), (c) June-July-August (JJA), and (d) September-October-November (SON). The crosses denote the regions where changes induced by SDE are statistically significant at 0.1 level.

**Figure 13.** As Figure 12, but for runoff change ( $\text{mm day}^{-1}$ ).

**Figure 14.** Seasonal evolution of runoff (left) and their change (right) in the Northern Rockies (top), the Greater Yellowstone region (center), and Southern Rockies (bottom). The unit is  $\text{mm day}^{-1}$ .

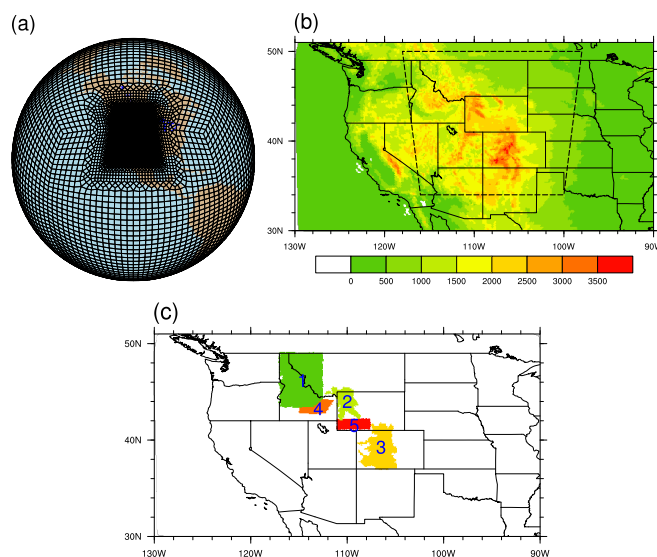
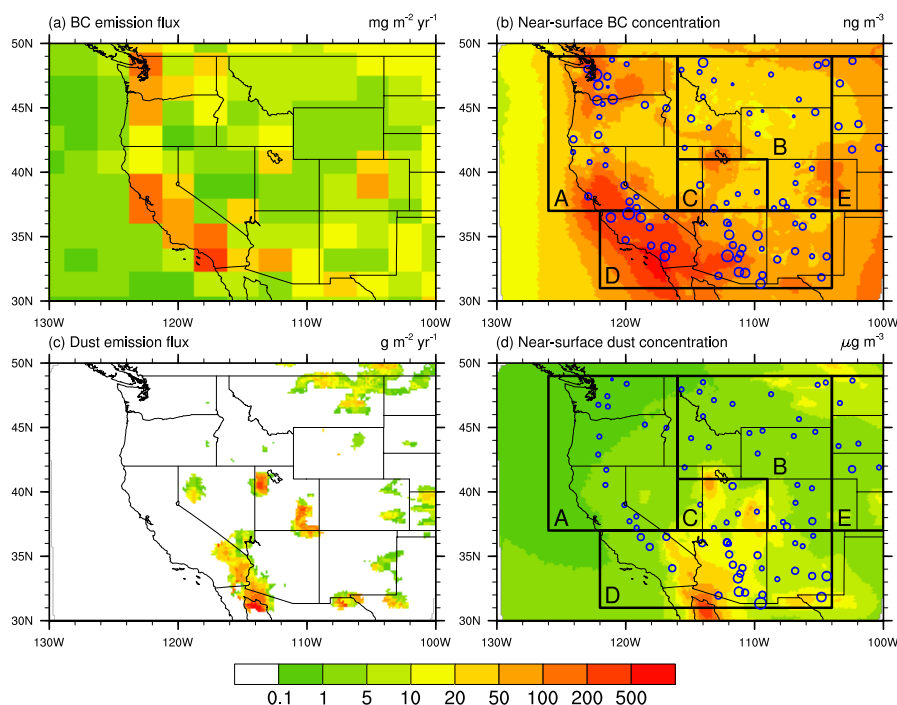


**Figure 1.** (a) Model meshes for variable resolution (uniform  $1^\circ$  with refined  $0.125^\circ$  in the Rocky Mountains) used in VR-CESM. Note that each element shown contains additional  $3 \times 3$  collocation gridcells. (b) Terrain height (m) in the western US with the refined region at a resolution of  $0.125^\circ$  surrounded by dashed lines. (c) Five regions identified for the analysis in this study, including three mountainous region (1, Northern Rockies; 2, Greater Yellowstone region; 3, Southern Rockies) and two regions in the plains around the mountains (4, Eastern Snake River Plain; 5, Southwestern Wyoming).



1058

1059



1060

1061 **Figure 2.** Spatial distribution of cold season (winter and spring) mean (a) BC  
 1062 emission flux and (b) near-surface BC concentration from the VR-CESM simulation;  
 1063 (c) and (d) for dust emission flux and near-surface dust concentration, respectively.  
 1064 Also shown are the IMPROVE stations (blue open circle) selected for model  
 1065 validation, with the size of the circles from small to large indicating the magnitude of  
 1066 observed near-surface BC/dust concentrations. The black rectangles in (b) and (d)  
 1067 denotes the five regions (A, West Coast; B, Rocky Mountains; C, Utah and Nevada;  
 1068 D, Southwestern US; E, Great Plain), which will be used to classify the stations in  
 1069 Figure 3. Note that units for BC and dust concentrations are  $\text{ng m}^{-3}$  and  $\mu\text{g m}^{-3}$ ,  
 1070 respectively.

1071

1072



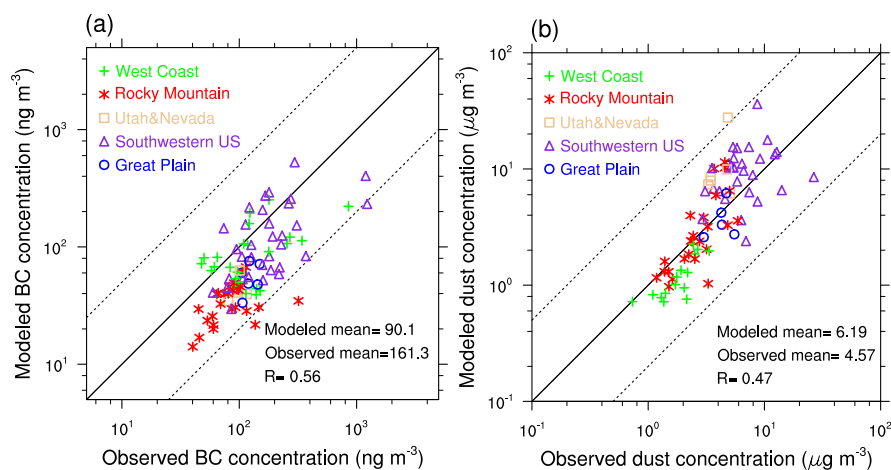
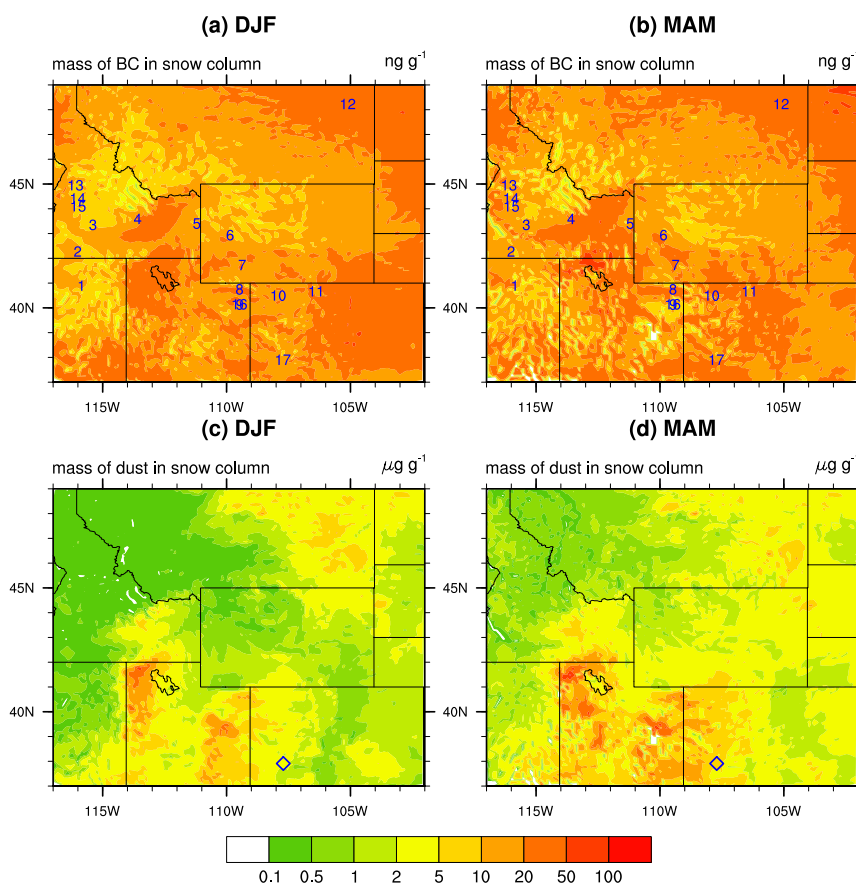


**Figure 3.** Comparison of cold season mean near-surface (a) BC and (b) dust concentrations at IMPROVE stations from VR-CESM simulation and IMPROVE observations. Also given are the mean results at all the stations from simulation and observations and their correlation coefficient ( $R$ ). The 1:1 (solid) and 1:5/5:1 (dash) lines are plotted for reference.



1083

1084 **Figure 4.** Winter (December-January-February (DJF); left) and spring

1085 (March-April-May (MAM); right) mean BC (upper row) and dust (bottom row) mass

1086 mixing ratios in snow column. Also shown are the stations for observations of BC

1087 mass in snow column (a, b) and for observations of dust mass in snow column at

1088 Senator Beck Basin Study Area (SBBSA) in the San Juan Mountains (c, d). Note that

1089 the units for BC and dust mass mixing ratios are given in different units, i.e.,  $\text{ng g}^{-1}$ 1090 and  $\mu\text{g g}^{-1}$ , respectively.

1091

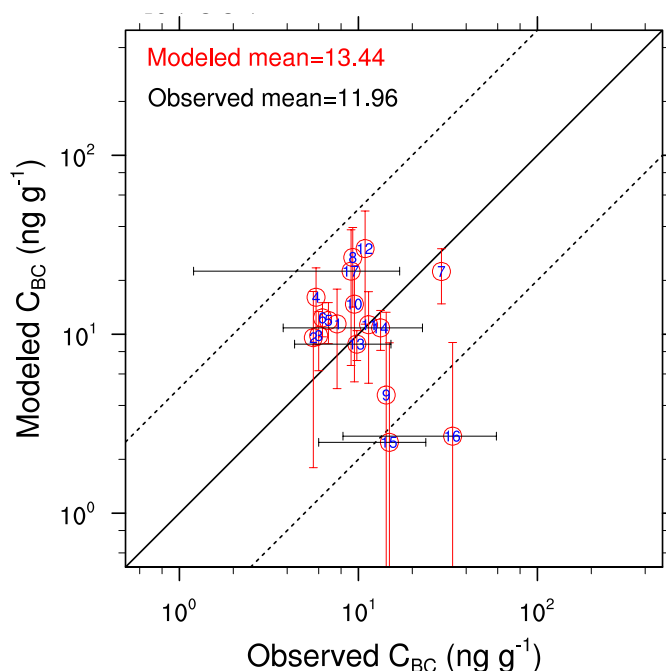
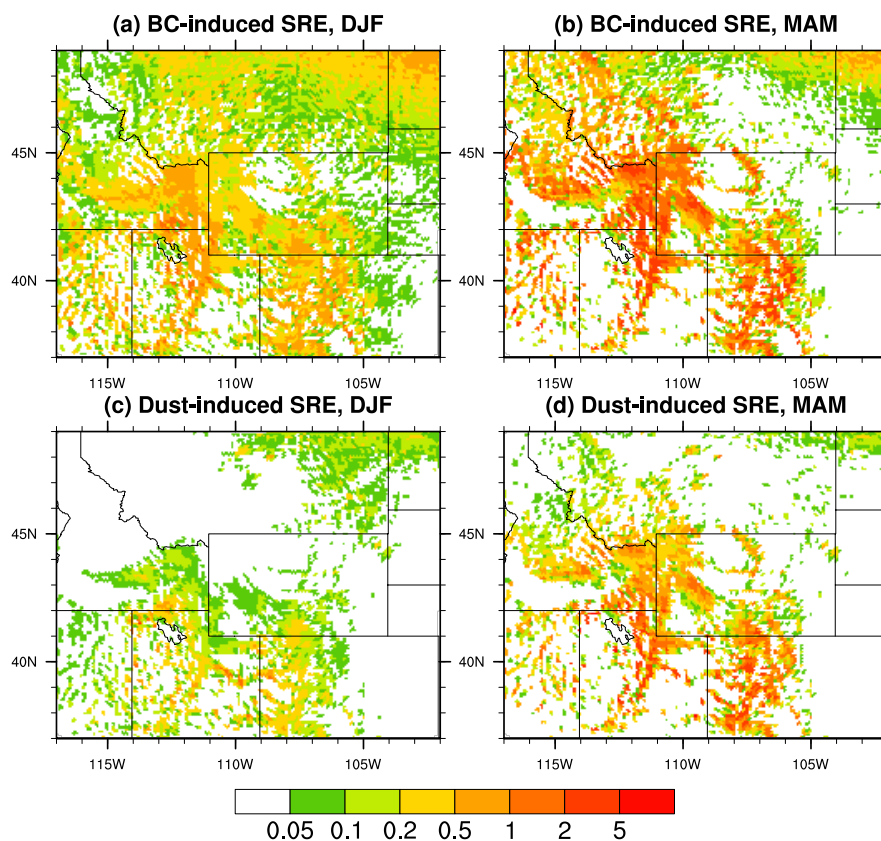


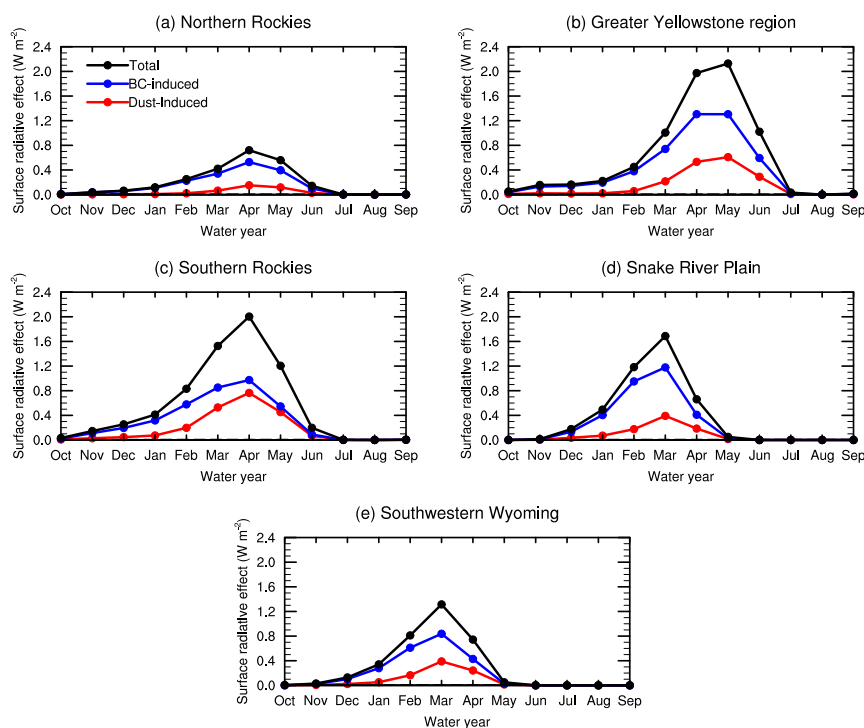
**Figure 5.** Comparison of BC mass concentrations in the snow column ( $C_{BC}$ ) at the 17 sites (see Table 1) from VR-CESM simulations and observations with the error bars denoting the corresponding standard deviations. The observations are compiled from the previously published studies (Table 1). If multiple observations are recorded at a certain site, the observed standard deviations are calculated from these multiple observations (section 3). Simulated BC mass concentration in the snow column and its standard deviation are calculated from the 25-year mean and standard deviation of simulation in the same month as the observations (section 3).



1105  
 1106 **Figure 6.** Winter (December-January-February (DJF), left) and spring  
 1107 (March-April-May (MAM), right) mean surface shortwave radiative effect (SRE,  $\text{W}$   
 1108  $\text{m}^{-2}$ ) induced by BC (top) and dust (bottom).  
 1109



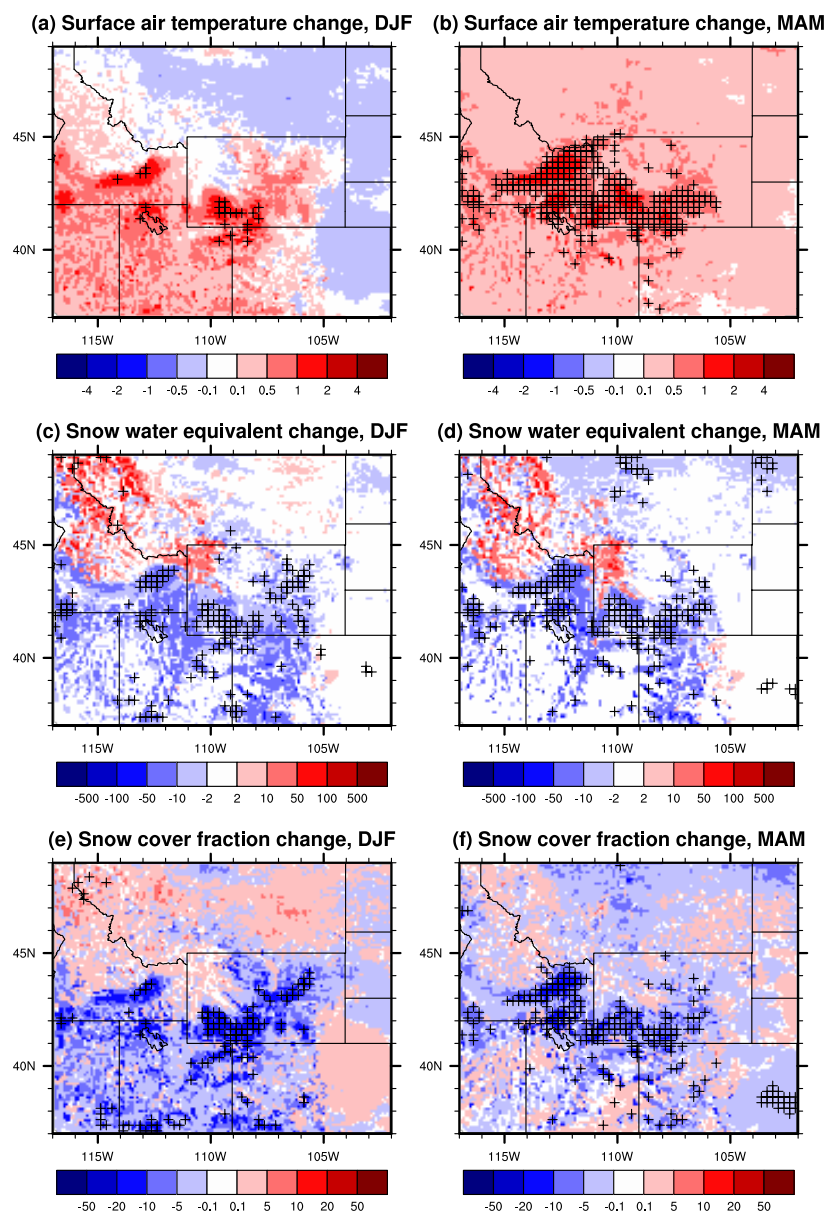
1110



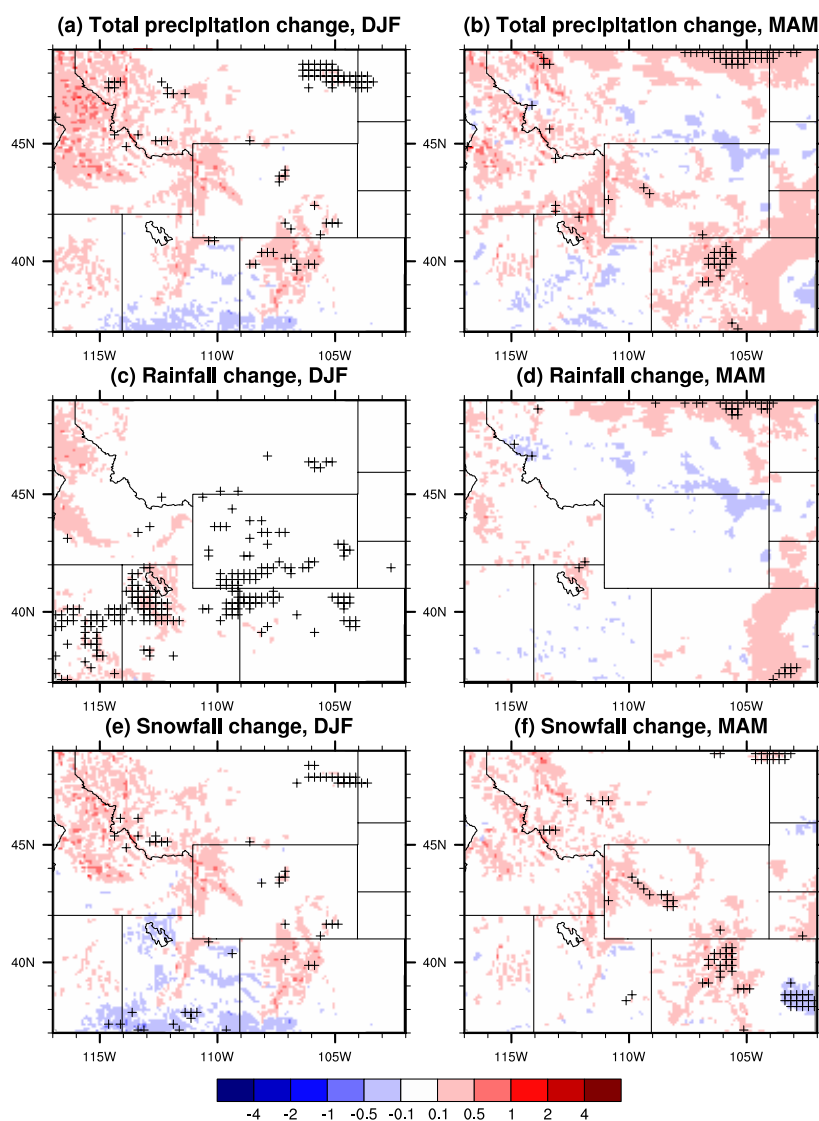
1111

1112 **Figure 7.** Monthly variations of surface radiative effect (SRE;  $\text{W m}^{-2}$ ) during the  
 1113 water year (October 1st to September 30th) averaged over the Northern Rockies,  
 1114 Greater Yellowstone region, Southern Rockies, Eastern Snake River Basin, and  
 1115 Southwestern Wyoming, respectively.

1116



1117  
 1118 **Figure 8.** Changes in surface air temperature (upper row; °C), snow water equivalent  
 1119 (bottom row; mm), and snow cover fraction (bottom row; %) in winter (left) and  
 1120 spring (right) induced by BC- and dust-in-snow. The crosses denote the regions where  
 1121 changes are statistically significant at 0.1 level.  
 1122



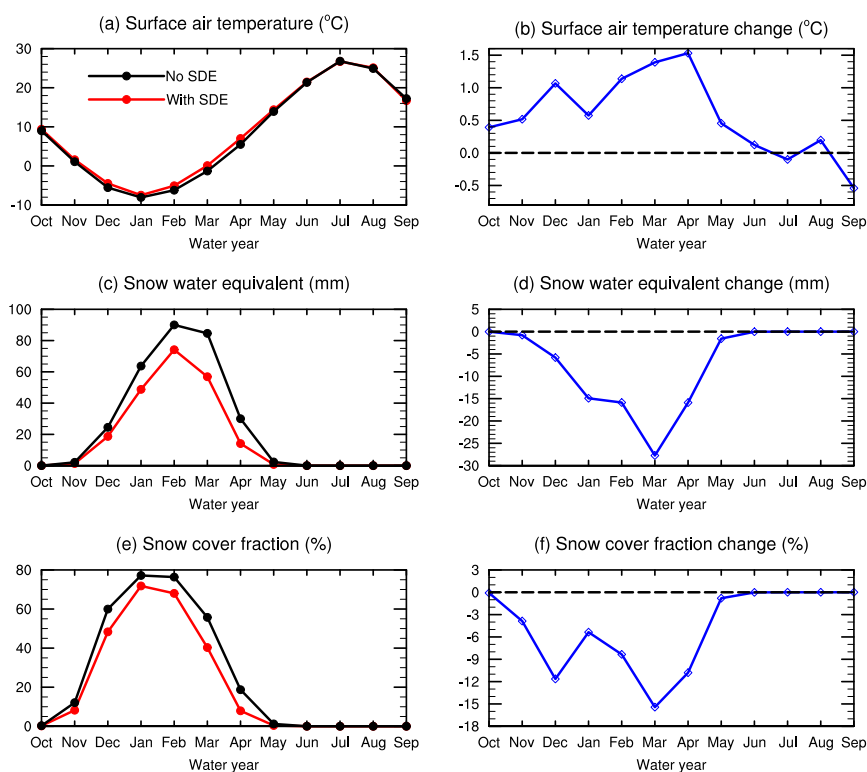
1123

1124 **Figure 9.** As Figure 8, but for total precipitation change (top), rainfall change (center),1125 and snowfall change (bottom). The unit is mm day<sup>-1</sup>.

1126

1127

1128



1129  
 1130 **Figure 10.** Seasonal evolution of (a) surface air temperature, (c) snow water  
 1131 equivalent, and (e) snow cover fraction and their changes due to SDE (b, d, and f)  
 1132 averaged over the Eastern Snake River Plain.  
 1133



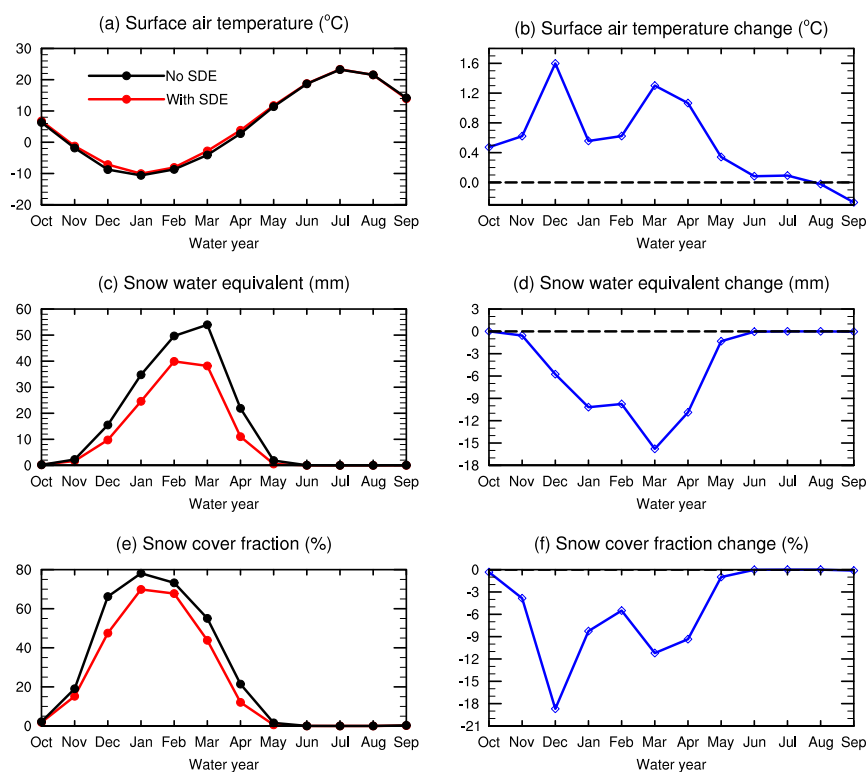
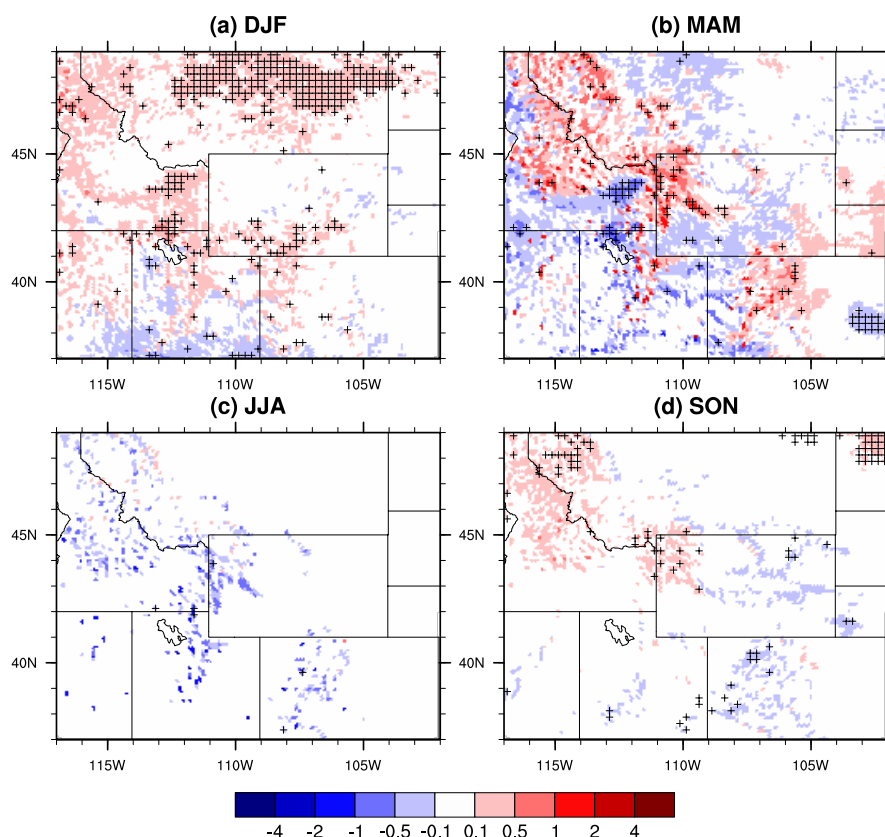


**Figure 11.** As Figure 10, but for Southwestern Wyoming.



1137

1138 **Figure 12.** Snowmelt change (mm day<sup>-1</sup>) due to SDE of BC and dust in four seasons:

1139 (a) December-January-February (DJF), (b) March-April-May (MAM), (c)

1140 June-July-August (JJA), and (d) September-October-November (SON). The crosses

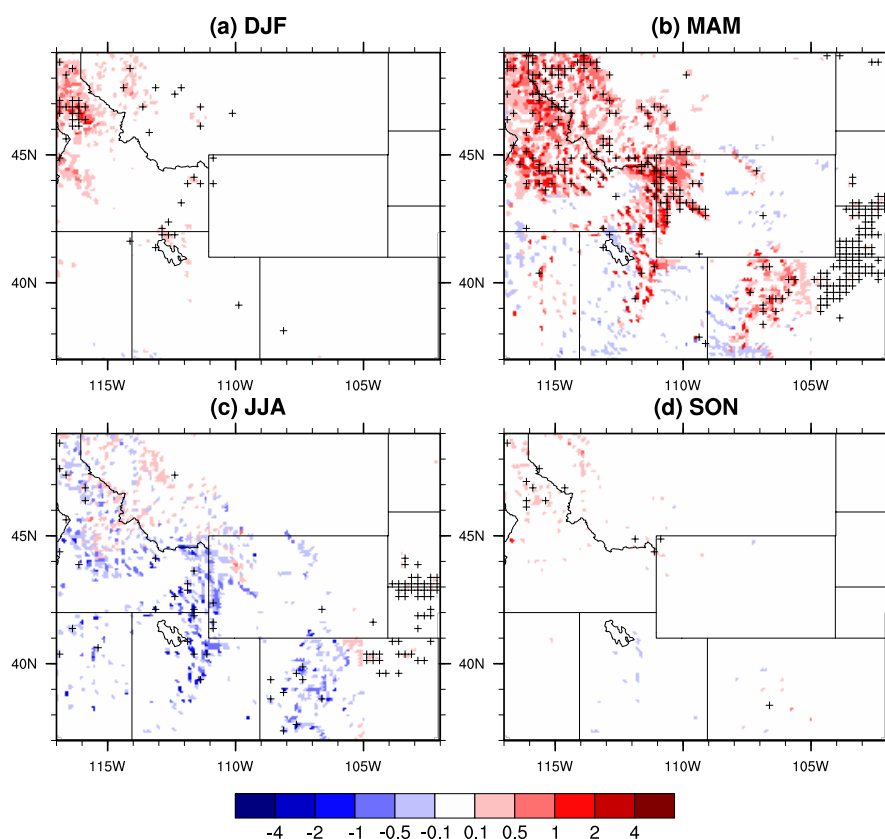
1141 denote the regions where changes induced by SDE are statistically significant at 0.1

1142 level.

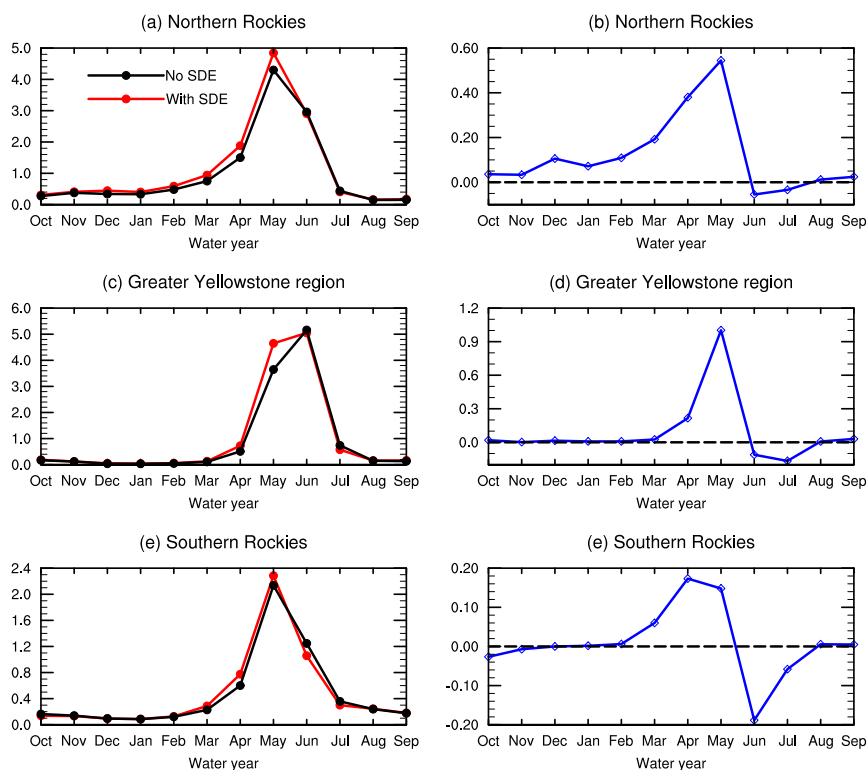
1143

1144

1145



1146  
 1147 **Figure 13.** As Figure 12, but for runoff change ( $\text{mm day}^{-1}$ ).  
 1148



1149  
1150 **Figure 14.** Seasonal evolution of runoff (left) and their change (right) in the Northern  
1151 Rockies (top), the Greater Yellowstone region (center), and Southern Rockies  
1152 (bottom). The unit is mm day<sup>-1</sup>.